A robotic system for automated genetic manipulation and analysis of *Caenorhabditis elegans* on agar media

Zihao Li[1,4], Anthony D. Fouad[1,4], Peter D. Bowlin[1], Yuying Fan[1], Siming He[1], Meng-Chuan Chang[1], Angelica Du[1], Christopher Teng[1], Alexander Kassouni[1], Hongfei Ji[1], David M. Raizen[2], and Christopher Fang-Yen[1,3]*

[1]Department of Bioengineering, University of Pennsylvania, Philadelphia, PA, USA.

[2]Department of Neurology, Perelman School of Medicine, University of Pennsylvania, Philadelphia, PA, USA.

[3]Department of Neuroscience, Perelman School of Medicine, University of Pennsylvania, Philadelphia, PA, USA.

[4]These authors contributed equally to this work.

*Correspondence should be addressed to C.F.-Y. (fangyen@seas.upenn.edu)

Abstract

The nematode *C. elegans* is one of the most widely studied organisms in biology due to its small size, rapid life cycle, and easily manipulated genetics. Research with *C. elegans* depends on labor-intensive and time-consuming manual procedures. Here we describe WormPicker, a robotic system capable of performing complex genetic manipulations and other tasks by imaging, phenotyping, and selectively

transferring *C. elegans* on standard agar media. Our system uses a motorized stage to move an imaging system and a robotic arm over an array of plates. Machine vision algorithms identify worms and assay their phenotypes, and the robotic arm transfers worms between plates using an electrically self-sterilized wire loop. We developed software to enable the system to autonomously carry out complex protocols. We validated the effectiveness and versatility of our methods by automating a collection of common *C. elegans* procedures, including genetic crossing, genetic mapping, and genomic integration of a transgene.

Introduction

Classical genetics, which investigates the heritability of traits across generations, usually requires manipulating reproductive behaviors of organisms and inferring their genetic properties by assaying their traits. The microscopic nematode *C. elegans* is one of the most widely used genetic models in the life sciences due to its easy maintenance, optical transparency, and rapid life cycle[1,2]. Studies in *C. elegans* have pioneered major fundamental advances in biology, including those in programmed cell death[3], aging[4], RNA interference[5], and axon guidance[6]. Work with worms has pioneered important techniques in modern biology including genome sequencing[7], cell lineage tracing[3], gene editing[8], electron microscopic reconstruction of neural connectivity[9], demonstration of green fluorescent protein[10], and optogenetic manipulation of neural activity[11].

42 Genetic manipulations in *C. elegans* are performed by manual procedures,
43 involving identification of animals under a microscope and transfer of worms or
44 embryos from one plate to another using a wire pick[12]. While manual procedures
45 are reliable and technically simple, they have important limitations.

46 Manual methods are labor intensive since they require animals to be
47 manipulated individually. This presents challenges to experiments that require
48 thousands of groups to be managed, for example conducting genetic screens[13],
49 working with collections of wild isolates[14], or dealing with mutagenized strains of the
50 Million Mutation Project[15].

51 During design of lab experiments, the use of manual procedures creates
52 practical limits to the number of conditions and the number of replicates for each
53 condition, weakening statistical power. Standard population sizes used for *C.*
54 *elegans* lifespan experiments have been shown to be underpowered for moderate
55 differences in lifespan between groups[16].

56 Finally, manual approaches require training and are prone to errors. This
57 reliance on investigator-learned skills imposes a barrier to entry for scientists without
58 *C. elegans* experience wishing to use this system.

59 To address the limitations of manual methods, automated high-throughput
60 genetic manipulations have been reported for bacteria and single cells in the field of
61 synthetic biology[17] and for adult *Drosophila*[18]. For work with *C. elegans*, methods for
62 automated imaging and sorting have been reported, including microfluidic devices[19-

[23] and flow-cell based sorting methods[24,25]. However, to our knowledge no methods for automated genetic manipulations in *C. elegans* have been reported.

Here we present WormPicker, a general-purpose robotic system allowing automated phenotyping and genetic manipulation of *C. elegans* on agar substrates, using comparable technique to current manual methods. Our method contains a 3D motorized stage carrying a robotic arm and an optical system. The robotic arm manipulates animals using a thin, electrically-sterilizable platinum wire loop. Analogous to manual methods, the robotic arm picks worms by performing spatially and temporally controlled motions above and on the agar surface, using food bacteria to encourage the worm to adhere to the loop. Contact between the platinum wire loop and the agar surface is perceived by a capacitive touch sensing circuit, providing feedback along with the imaging system for fine adjustment of the pick trajectory relative to the animal.

The optical system is capable of monitoring animals over an entire plate at low magnification (6 cm diameter circular field of view (FOV)) while simultaneously imaging individual animals at high magnification (1.88 mm x 1.57 mm FOV) to obtain more detailed morphological and/or fluorescence information. Using machine vision methods, worms can be recognized and tracked over the plates in low magnification and undergo detailed phenotyping in high magnification across different attributes, including developmental stage, morphology, sex, and fluorescence expression. We developed system control software (WormPickerControl) through which the user can specify multi-step genetic procedures to be performed by the automated system.

Using these automated tools, we successfully carried out three genetic procedures commonly performed in *C. elegans* research. First, we generated a genetic cross between transgenic and mutant animals using a classic genetic hybridization scheme. Second, we performed genetic mapping of a genome-integrated fluorescent transgene. Finally, we integrated an extrachromosomal transgenic array to the genome, creating a stable transgenic line. Successful completion of these complex genetic procedures demonstrates WormPicker's effectiveness and versatility as a general-purpose automated tool for *C. elegans* genetics.

Results

Overview of WormPicker system design

Our system contains a robotic picking arm, optical imaging system, lid manipulators, and other elements, mounted on a 3-dimensional motorized stage to work with an array of up to 144 plates (Fig. 1a-b, Supplementary Fig. 1).

The array of agar plates is housed on a platform (Fig. 1b), containing 8 trays that can be prepared separately and then slid into the automated system (Methods, Supplementary Fig. 2a,b). Each plate on the tray is labeled with an adhesive bar code and text (Fig. 1a, Supplementary Fig. 2c-d). We developed software to track plates during experiments using their barcode identifiers (Methods, Supplementary Fig. 2g-i).

The imaging system is designed for bright-field and fluorescence imaging through low- (0.035X) and high-magnification (10X) optical pathways. The low-magnification stream is of a 6 cm diameter circular field of view (FOV), capable of imaging one 6 cm diameter plate; the high-magnification has a 1.88 mm x 1.57 mm FOV, capable of imaging individual animals in detail. For bright-field imaging, light is collected by the main objective and divided into low and high magnification imaging streams by a beam splitter (Supplementary Fig. 3a). For fluorescence imaging, collimated excitation LEDs (center wavelengths 470 nm and 565 nm) and a fluorescence optics (Supplementary Fig. 3b-c) enable imaging in green (503 – 541 nm wavelength) and red (606 – 661 nm wavelength) channels (Supplementary Video 1) in the high magnification pathway.

To quickly bring a plate into focus, we use a laser-based autofocusing system (Fig. 1a, Methods, Supplementary Fig. 3d). A 532 nm laser pointer with a cylindrical lens generates a line projected onto the agar surface from an oblique angle, providing feedback for the motorized stage to bring the imaging system to the correct position.

Plate lids are manipulated by a vacuum gripping system (Fig. 1a, Methods, Supplementary Fig. 3e). Two lid handlers are mounted to either side of the main motorized gantry, for manipulating lids for a source plate and a destination plate separately (only one shown in Fig. 1a). Each vacuum lid gripper is raised and lowered by a motorized linear actuator (Supplementary Video 2).

127 The robotic picking arm (Fig. 1a, Supplementary Fig. 3f) contains a motorized
128 linear actuator for fine adjustment of the pick's height and three servo motors to
129 provide rotational degrees of freedom. The 3D-printed pick contains a platinum wire
130 loop attached to its end (Fig. 1c), for manipulating *C. elegans* in a manner analogous
131 to manual methods[12].

132 Conventional pick sterilization prior to manipulating *C. elegans* on agar
133 substrates requires an open flame, which poses safety risks in an automated
134 system. We adopted an electric sterilization approach (Fig. 1c) in which a current is
135 passed through the wire loop to sterilize it via resistive heating (Supplementary
136 Video 3).

137 Picking up *C. elegans* requires very fine control of the position of the pick to
138 avoid damage to the worm or the agar surface. While the horizontal position of the
139 pick can be monitored by the imaging system, its height relative to the agar surface
140 is more difficult to determine. To address this problem, we developed a capacitive
141 touch sensing circuit (Supplementary Fig. 3g), that monitors contact between the
142 platinum wire and agar surface and provides feedback for fine tuning the pick's
143 movements.

144 To pick up a worm (Fig. 1d), the wire pick is positioned above the agar (IP), with
145 a horizontal offset to the target worm. The linear stepper actuator lowers the pick
146 until contacting the agar surface (TP) as perceived by the capacitive touch sensor
147 (Phase A). Next, Servo 2 horizontally swipes the pick on the agar surface (Phase

148 B). Servos 1 and 3 act simultaneously to perform a curved motion (Phase C) for
149 picking up the target animal using the outer side of the wire loop. To release the
150 worm from the pick to the substrate (Fig. 1e), the pick is positioned above the
151 substrate (IP); the linear stepper actuator vertically lowers (Phase A) the pick until it
152 touches the agar (TP); the Servo 2 horizontally swipes (Phase B) the pick on the
153 agar surface horizontally, to release the worm from the pick. Supplementary Video 4
154 depicts these operations as observed by the imaging system.

155

156 Machine vision enables automated identification and phenotyping

157 We developed machine vision analysis software for the low- and high-
158 magnification streams.

159 We analyze the low-magnification images (Fig. 2a) using a combination of a
160 convolutional neural network (CNN) and motion detection for tracking worms and the
161 pick in real time. High-magnification bright-field images (Fig. 2b) are analyzed by a
162 set of Mask-Regional CNNs (Mask-RCNNs)[26] capable of performing pixel-wise
163 object segmentations. Contours of individual animals are segmented by a Mask-
164 RCNN (Fig. 2b), and the contour geometries are analyzed for developmental stage
165 and morphology. In addition, we trained separate networks for sex determination
166 and embryo detection. Inferences from multiple Mask-RCNNs are integrated for
167 assaying phenotypes for individual animals over different attributes.

168 For high-magnification fluorescence imaging (Fig. 2c), we first apply intensity
169 analysis, through which valid fluorescence regions are extracted from the
170 background. To analyze fluorescence expression the fluorescence images are
171 correlated with the animal contours segmented using the bright-field images, (Fig.
172 2c).

173 For details of machine vision approaches see Methods and Supplementary Fig.
174 5.

175

176 Automated throughput is comparable to that of experienced
177 researchers

178 To compare the speeds of automated and manual picking, we evaluated the
179 rates at which the robot and human researchers perform a fluorescent animal sorting
180 task. We used a strain in which some but not all worms carry a *myo-2::GFP*-
181 labeled fluorescent extrachromosomal array (YX256); the task was to sort these
182 worms into two plates containing fluorescent and nonfluorescent animals.

183 The robotic system sorted the animals (mixed stages) with a throughput of 3.21
184 ± 0.66 (mean ± SD) animals per minute (APM).

185 We recruited a group of *C. elegans* researchers (N = 21) to perform the same
186 task using standard methods. The mean and median of the years of experience
187 were 7.61 and 5 years. We tasked each volunteer to sort approximately 20 animals
188 (of mixed stages) using a regular platinum wire pick[12] under a fluorescence stereo

microscope. The measured throughputs are plotted versus years of experience in Supplementary Fig. 6. The manual picking throughput was 3.56 ± 1.67 (mean ± SD) APM. Both WormPicker and the researchers picked individual worms and sterilized the pick between transfers.These results show that the throughput of our robotic system for this fluorescence worm sorting task is comparable to that of experienced human researchers.

Scripting toolsets enable complex genetic manipulations

In order for WormPicker to be useful for practical laboratory work, the basic elements of identifying and transferring worms need to be combined to form complex genetics procedures. To that end, we developed system control software, WormPickerControl (Supplementary Fig. 7a). An Application Programming Interface (API) enables the user to write scripts for specifying *C. elegans* procedures to be carried out by the automated system. We developed a library of source scripts, each responsible for a specific task ranging from simple to complex. We constructed a database through which the automated system is able to catalog a set of plates throughout the experiments based on the machine vision readable unique barcode identifiers (Fig. 1a, Supplementary Fig. 2).

Using WormPickerControl, we developed and tested a collection of genetic procedures commonly undertaken in *C. elegans* labs (Fig. 3, 4, and 5). These are

209 not intended to be a complete set of genetic protocols, but rather to provide a useful
210 initial framework that can be modified and adapted to other experiments as needed.

211

212 **Automated genetic cross**

213 The genetic cross, by which two or more mutations or transgenes are combined,
214 is performed by placing males together with hermaphrodites on the agar surface of a
215 Petri dish[27]. While monitoring the plates, researchers pick cross-progeny with
216 desired phenotypes. Most genetic crosses require manipulating animals over
217 multiple generations.

218 We automated a genetic cross between two *C. elegans* strains: *dop-1p::GFP*
219 fluorescent transgenic (LX831) and a *dpy-5(e61)* mutant (CB61) (Fig. 3). The LX831
220 strain contains an integrated transgene *vsIs28 [dop-1p::GFP]* and has a green
221 fluorescent phenotype: GFP expressed in several cell types including some neurons
222 and muscles (Fig. 3a). The *dpy-5* mutant has a Dumpy (Dpy) phenotype,
223 characterized by a morphology that is shorter and stouter than wild-type animals
224 (Fig. 3b). The *vsIs28* transgene is dominant (i.e. both heterozygotes and
225 homozygotes show green fluorescence) whereas the *dpy-5* mutation is recessive
226 (i.e. only the homozygotes show the Dpy phenotype). The resulting hybridized strain
227 displays both phenotypes of two parental strains, i.e., it is both Green and Dpy (Fig.
228 3c).

229 Fig. 3d depicts the genetic cross. WormPicker picked 17 L4 males from an N2
230 wild-type population that consisted of a mixture of males and hermaphrodites. It also
231 picked 4 L4 hermaphrodites from the LX831 strain to the same plates. Green males
232 were visible in the progeny, indicating that the mating was successful. Next, six
233 Green L4 *vsIs28* heterozygous males and two *dpy-5* homozygous L4
234 hermaphrodites were picked onto a plate for mating. We consider this mating the
235 parental (P0) generation.

236 Filial generation 1 (F1) progeny included animals that were Green and not Dpy.
237 These were the desired worms heterozygous for both *vsIs28* and *dpy-5* and were
238 therefore transferred by WormPicker to fresh plates. The automated system
239 screened over the plate and singled two F1 hermaphrodites with the wanted
240 phenotypes.

241 Four phenotypes were observed in the F2 generation, including Dpy-Green,
242 Dpy-non-Green, non-Dpy-Green, and non-Dpy-non-Green. The frequency of desired
243 Dpy-Green phenotype was ~10%. WormPicker inspected the F2 populations and
244 singled 3 Dpy-Green animals.

245 F3 populations descending from each of the three F2s were 100% Dpy but only
246 75% Green indicating that they were homozygous for *dpy-5* but heterozygous for
247 *vsIs28*. WormPicker then singled 11 Dpy-Green worms.

248 The automated system screened for percentages of Green F5s descending from
249 each of eleven F4s and identified one line displaying homozygous fluorescent, i.e.,
250 100% of F5s were Green.

251 The results were verified manually by an experienced *C. elegans* researcher by
252 noting that the resulting strain was positive for both Green and Dpy phenotypes, and
253 that these phenotypes bred true in subsequent generations.

254

255 Automated genetic mapping of a transgene

256 The identification of the genotype causing a particular phenotype usually
257 requires genetic linkage analysis. The first step in such analysis is the identification
258 of the chromosomes harboring the genetic change.

259 *C. elegans* has six chromosomes, of which five are autosomes and one is the X
260 chromosome. Hermaphrodites are diploid for all of six chromosomes, while males
261 are diploid for five autosomes and haploid for the X chromosome.

262 Genetic mapping in *C. elegans* can be performed by setting up genetic crosses
263 between the strain of interest and a set of marker strains, and measuring the
264 segregation pattern between the marker phenotypes and the phenotype of interest.

265 We used WormPicker to perform an automated genetic mapping of an integrated
266 red fluorescent transgene *vsIs33 [dop-3p::RFP]* (LX811) (Fig. 4). This strain has a
267 Red phenotype, i.e. RFP is expressed in cells expressing the DOP-3 dopamine
268 receptors (Fig. 4a).

269 We evaluated the linkage of *vsIs33* to autosomes by setting up crosses between
270 our strain of interest (LX811) and a set of balancer strains. These balancer strains
271 are labeled by *myo-2::GFP* markers and have a Green phenotype (GFP expressed
272 in pharyngeal muscles) (Fig. 4b). We used the reciprocal translocations *hT2*[28] *[qIs48]*
273 *(I;III)*, *eT1*[29,30] *[umnIs12] (III;V)*, and *nT1*[31-33] *[qIs51] (IV;V)* to test for linkage to large
274 portions of chromosomes I and III, III and V, and IV and V, respectively. We used the
275 inversion *mIn1*[34] *[mIs14] (II)*, to test for linkage to chromosome II (Fig. 4c,
276 Supplementary Fig. 8-11, Methods).

277 WormPicker picked L4 Green males from the balancer strains and
278 hermaphrodites from the strain of interest (LX811) for mating. WormPicker then
279 screened for F1 Red-Green hermaphrodites, a few of which were subsequently
280 singled. The double-fluorescent F1 hermaphrodites self-fertilized and produced F2s,
281 where the percentages of Red among non-Green animals were assessed to test for
282 linkage between *vsIs33* and particular autosomes. According to classic genetic
283 theory, linkage of the transgene to the tested balancer chromosomes would yield
284 100% of non-Green animals to be Red, whereas non-linkage of the transgene to the
285 balancer would be reflected by 75% Red among non-Green progeny.

286 For testing linkage to the X chromosome, WormPicker generated a genetic cross
287 between LX811 hermaphrodites and wild-type males harboring a dominant
288 extrachromosomal transgene *qnEx615 [myo-2p::GFP]* (NQ1155) (Methods), which
289 helped us to identify F1 cross-progeny. As shown in Fig. 4c, F1 Red-Green males
290 were picked out for mating with N2 (wild-type) hermaphrodites. F2s were screened

291 by the robotic system, and the observed percentage of Red among males was used
292 for quantifying the degree to which *vsIs33* is linked to the X chromosome. The theory
293 predicts that none of the F2 males would be Red if X-linked, and that 50% of the F2
294 males would be Red if not X-linked (Supplementary Fig. 12).

295 To quantify the strength of linkage we defined a linkage Index ranging from -1 to
296 1, where 1 implies the strongest possible linkage and 0 the weakest (Fig. 4d). Our
297 data indicated strong linkage of *vsIs33* both to *eT1* and *nT1*, and no linkage to *hT2*,
298 to *mIn1*, or to the X chromosome. Since both *eT1* and *nT1* balance a large portion of
299 chromosome V, our results imply that the RFP transgene is located on chromosome
300 V.

301

302 **Genomic integration of a transgene**

303 Transgenic *C. elegans* are usually generated by microinjection, through which
304 cloned DNAs can be delivered to the distal gonadal arm, forming extrachromosomal
305 transgenic arrays[35,36]. To provide stable inheritance and expression the transgenic
306 arrays can be integrated to the genome. A proven method for genomic integration
307 is to irradiate the strain of interest, causing breakage in chromosomes, which
308 triggers DNA repair, a process through which the transgenic arrays can be ligated to
309 the chromosomes by chance[35]. Due to the low frequency of integration events,
310 identifying animals with transgene integrated requires isolating at least several
311 hundred individual worms and screening for 100% inheritance of the transgene in

312 subsequent generations, a highly labor-intensive task[37]. In particular, the need to
313 single hundreds of animals can consume a substantial amount of time, even for
314 experienced *C. elegans*.

315 Using WormPicker, we performed a genomic integration of an *acr-2p::DOP-3*
316 extrachromosomal array labeled by a green fluorescent marker *unc-47p::GFP*
317 (YX293) (Fig. 5). The strain displayed approximately 65% transmission of the
318 transgenic arrays to the next generation. To create the P0 worms, we irradiated 68
319 L4s with ultraviolet light (254 nm, 30 mJ/cm^2). WormPicker isolated 216 F1s to
320 individual plates. From these plates, the automated system isolated 612 of their
321 progeny (F2s) to individual plates. The F2 animals were manually screened for
322 100% transmission of the transgene to F3s and F4s. Among those, two lines were
323 identified as true independent integrants.

324

325 Discussion

326 In this work, we have demonstrated that WormPicker can automate a variety of
327 *C. elegans* genetics procedures usually performed by manual methods. In addition,
328 our user-friendly scripting tools provide flexibility for carrying out customized
329 experiments as well as integrating the robotic system into diverse genetic screens
330 and analyses, potentially including pharmacological screening[38,39], screening for
331 aging phenotypes[4,40,41], and studies of natural genetic variation[42].

The deep-learning-aided machine vision methods we developed here, capable of segmenting individual animals and assaying them across different attributes, may find other applications for *C. elegans* studies, for example in analyses of locomotion[43,44], aging[45,46], and sleep[47].

Our self-sterilizing loop design can be used for automatically manipulating other microscopic organisms, for example other nematodes, *Drosophila* larvae, bacteria, and fungi.

It Is important to acknowledge the limitations of our work. For a simple fluorescent animal sorting task, the throughput achieved by WormPicker with a single robotic arm was somewhat smaller than the average of that of experienced researchers. However, it has the advantage of being able to work continuously without fatigue and to conduct a large number of operations in parallel.

Worms sometimes cluster together in a way that makes it difficult to pick a single individual. We have demonstrated that WormPicker's machine vision is able to segment individual animals in high-resolution images on highly populated plates (Supplementary Fig. 6d). For the experiments presented here, we programmed the robot to perform intermediate picking (Methods) before transferring worms to their destinations, as a method of handling clusters of animals. In addition, brief blue light illumination[45,49] or plate vibration could be used to disperse clusters of animals.

Although WormPicker's machine vision system works well for worm recognition and tracking for the wild-type and dumpy strains involved here, the current

algorithms trained on wild-type worms may not be effective for some mutants with unusual morphologies.

We expect all worm manipulations will continue to involve some degree of manual work in conjunction with the automated system. The researcher must prepare plates, load and unload them on the trays, and select the appropriate operations. The effective integration of WormPicker to lab work will require determining which genetic operations are most amenable to automation and which are better left to manual work. The goal of our work is not to fully automate experiments, in the sense that the human is no longer needed, but rather to provide tools to increase the productivity of the researcher.

References

1 Brenner, S. The genetics of Caenorhabditis elegans. *Genetics* **77**, 71-94 (1974).

2 Corsi, A. K., Wightman, B. & Chalfie, M. A transparent window into biology: a primer on Caenorhabditis elegans. *Genetics* **200**, 387-407 (2015).

3 Sulston, J. E. & Horvitz, H. R. Post-embryonic cell lineages of the nematode, Caenorhabditis elegans. *Developmental biology* **56**, 110-156 (1977).

4 Kenyon, C., Chang, J., Gensch, E., Rudner, A. & Tabtiang, R. A C. elegans mutant that lives twice as long as wild type. *Nature* **366**, 461-464 (1993).

5 Fire, A. *et al.* Potent and specific genetic interference by double-stranded RNA in Caenorhabditis elegans. *nature* **391**, 806-811 (1998).

6 Chisholm, A. D., Hutter, H., Jin, Y. & Wadsworth, W. G. The genetics of axon guidance and axon regeneration in Caenorhabditis elegans. *Genetics* **204**, 849-882 (2016).

7 Consortium*, C. e. S. Genome sequence of the nematode C. elegans: a platform for investigating biology. *Science* **282**, 2012-2018 (1998).

8 Wood, A. J. *et al.* Targeted genome editing across species using ZFNs and TALENs. *Science* **333**, 307-307 (2011).

9 Cook, S. J. *et al.* Whole-animal connectomes of both Caenorhabditis elegans sexes. *Nature* **571**, 63-71 (2019).

10 Chalfie, M., Tu, Y., Euskirchen, G., Ward, W. W. & Prasher, D. C. Green fluorescent protein as a marker for gene expression. *Science* **263**, 802-805 (1994).

11 Fang-Yen, C., Alkema, M. J. & Samuel, A. D. Illuminating neural circuits and behaviour in Caenorhabditis elegans with optogenetics. *Philosophical Transactions of the Royal Society B: Biological Sciences* **370**, 20140212 (2015).

12 Stiernagle, T. Maintenance of C. elegans. (1999).

13 Jorgensen, E. M. & Mango, S. E. The art and design of genetic screens: Caenorhabditis elegans. *Nature Reviews Genetics* **3**, 356-369 (2002).

394 14 Cook, D. E., Zdraljevic, S., Roberts, J. P. & Andersen, E. C. CeNDR, the
395 Caenorhabditis elegans natural diversity resource. *Nucleic acids research* **45**,
396 D650-D657 (2017).
397 15 Thompson, O. *et al.* The million mutation project: a new approach to genetics
398 in Caenorhabditis elegans. *Genome research* **23**, 1749-1762 (2013).
399 16 Petrascheck, M. & Miller, D. L. Computational analysis of lifespan experiment
400 reproducibility. *Frontiers in genetics* **8**, 92 (2017).
401 17 Wang, H. H. *et al.* Programming cells by multiplex genome engineering and
402 accelerated evolution. *Nature* **460**, 894-898 (2009).
403 18 Alisch, T., Crall, J. D., Kao, A. B., Zucker, D. & de Bivort, B. L. MAPLE
404 (modular automated platform for large-scale experiments), a robot for
405 integrated organism-handling and phenotyping. *Elife* **7**, e37166 (2018).
406 19 Crane, M. M. *et al.* Autonomous screening of C. elegans identifies genes
407 implicated in synaptogenesis. *Nature methods* **9**, 977-980 (2012).
408 20 Ben-Yakar, A., Chronis, N. & Lu, H. Microfluidics for the analysis of behavior,
409 nerve regeneration, and neural cell biology in C. elegans. *Current opinion in*
410 *neurobiology* **19**, 561-567 (2009).
411 21 Rohde, C. B., Zeng, F., Gonzalez-Rubio, R., Angel, M. & Yanik, M. F.
412 Microfluidic system for on-chip high-throughput whole-animal sorting and
413 screening at subcellular resolution. *Proceedings of the National Academy of*
414 *Sciences* **104**, 13891-13895 (2007).

22 Atakan, H. B., Alkanat, T., Cornaglia, M., Trouillon, R. & Gijs, M. A. Automated phenotyping of Caenorhabditis elegans embryos with a high-throughput-screening microfluidic platform. *Microsystems & Nanoengineering* **6**, 1-14 (2020).

23 Chung, K., Crane, M. M. & Lu, H. Automated on-chip rapid microscopy, phenotyping and sorting of C. elegans. *Nature methods* **5**, 637-643 (2008).

24 Pulak, R. Techniques for analysis, sorting, and dispensing of C. elegans on the COPAS™ flow-sorting system. *C. elegans*, 275-286 (2006).

25 Doitsidou, M., Flames, N., Lee, A. C., Boyanov, A. & Hobert, O. Automated screening for mutants affecting dopaminergic-neuron specification in C. elegans. *Nature methods* **5**, 869-872 (2008).

26 He, K., Gkioxari, G., Dollár, P. & Girshick, R. in *Proceedings of the IEEE international conference on computer vision.* 2961-2969.

27 Fay, D. Genetic mapping and manipulation: Chapter 1-Introduction and basics. *WormBook* **17**, 1-12 (2006).

28 McKim, K. S., Peters, K. & Rose, A. M. Two types of sites required for meiotic chromosome pairing in Caenorhabditis elegans. *Genetics* **134**, 749-768 (1993).

29 Rosenbluth, R. E. & Baillie, D. L. The genetic analysis of a reciprocal translocation, eT1 (III; V), in Caenorhabditis elegans. *Genetics* **99**, 415-428 (1981).

436 30 Rosenbluth, R. E., Cuddeford, C. & Baillie, D. L. Mutagenesis in
437 Caenorhabditis elegans. II. A spectrum of mutational events induced with
438 1500 r of γ-radiation. *Genetics* **109**, 493-511 (1985).
439 31 Ferguson, E. L. & Horvitz, H. R. Identification and characterization of 22
440 genes that affect the vulval cell lineages of the nematode Caenorhabditis
441 elegans. *Genetics* **110**, 17-72 (1985).
442 32 Clark, D. V., Rogalski, T. M., Donati, L. M. & Baillie, D. L. The unc-22 (IV)
443 region of Caenorhabditis elegans: genetic analysis of lethal mutations.
444 *Genetics* **119**, 345-353 (1988).
445 33 Rogalski, T. M. & Riddle, D. L. A Caenorhabditis elegans RNA polymerase II
446 gene, ama-1 IV, and nearby essential genes. *Genetics* **118**, 61-74 (1988).
447 34 Edgley, M. & Riddle, D. LG II balancer chromosomes in Caenorhabditis
448 elegans: mT1 (II; III) and the mIn1 set of dominantly and recessively marked
449 inversions. *Molecular Genetics and Genomics* **266**, 385-395 (2001).
450 35 Evans, T. C. Transformation and microinjection. *WormBook* **10** (2006).
451 36 Mello, C. C., Kramer, J. M., Stinchcomb, D. & Ambros, V. Efficient gene
452 transfer in C. elegans: extrachromosomal maintenance and integration of
453 transforming sequences. *The EMBO journal* **10**, 3959-3970 (1991).
454 37 Mariol, M.-C., Walter, L., Bellemin, S. & Gieseler, K. A rapid protocol for
455 integrating extrachromosomal arrays with high transmission rate into the C.
456 elegans genome. *JoVE (Journal of Visualized Experiments)*, e50773 (2013).

457 38 Kaletta, T. & Hengartner, M. O. Finding function in novel targets: C. elegans
458 as a model organism. *Nature reviews Drug discovery* **5**, 387-399 (2006).
459 39 Chen, A. L. *et al.* Pharmacological convergence reveals a lipid pathway that
460 regulates C. elegans lifespan. *Nature chemical biology* **15**, 453-462 (2019).
461 40 Hamilton, B. *et al.* A systematic RNAi screen for longevity genes in C.
462 elegans. *Genes & development* **19**, 1544-1555 (2005).
463 41 Garigan, D. *et al.* Genetic analysis of tissue aging in Caenorhabditis elegans:
464 a role for heat-shock factor and bacterial proliferation. *Genetics* **161**, 1101-
465 1112 (2002).
466 42 Frézal, L., Demoinet, E., Braendle, C., Miska, E. & Félix, M.-A. Natural
467 genetic variation in a multigenerational phenotype in C. elegans. *Current*
468 *Biology* **28**, 2588-2596. e2588 (2018).
469 43 Yemini, E., Jucikas, T., Grundy, L. J., Brown, A. E. & Schafer, W. R. A
470 database of Caenorhabditis elegans behavioral phenotypes. *Nature methods*
471 **10**, 877-879 (2013).
472 44 Bates, K., Le, K. N. & Lu, H. Deep learning for robust and flexible tracking in
473 behavioral studies for C. elegans. *PLOS Computational Biology* **18**, e1009942
474 (2022).
475 45 Churgin, M. A. *et al.* Longitudinal imaging of Caenorhabditis elegans in a
476 microfabricated device reveals variation in behavioral decline during aging.
477 *Elife* **6**, e26652 (2017).

478 46 Stroustrup, N. *et al.* The Caenorhabditis elegans lifespan machine. *Nature*
479 *methods* **10**, 665-670 (2013).
480 47 Raizen, D. M. *et al.* Lethargus is a Caenorhabditis elegans sleep-like state.
481 *Nature* **451**, 569-572 (2008).
482 48 McClanahan, P. D., Xu, J. H. & Fang-Yen, C. Comparing Caenorhabditis
483 elegans gentle and harsh touch response behavior using a multiplexed
484 hydraulic microfluidic device. *Integrative Biology* **9**, 800-809 (2017).
485 49 Edwards, S. L. *et al.* A novel molecular solution for ultraviolet light detection in
486 Caenorhabditis elegans. *PLoS biology* **6**, e198 (2008).
487 50 Leifer, A. M., Fang-Yen, C., Gershow, M., Alkema, M. J. & Samuel, A. D.
488 Optogenetic manipulation of neural activity in freely moving Caenorhabditis
489 elegans. *Nature methods* **8**, 147-152 (2011).
490 51 Byerly, L., Cassada, R. & Russell, R. The life cycle of the nematode
491 Caenorhabditis elegans: I. Wild-type growth and reproduction. *Developmental*
492 *biology* **51**, 23-33 (1976).
493 52 Wb, B. S. W. The nematode Caenorhabditis elegans. *Cold Spring Harbor*
494 *Laboratory* **1**, 1091-1105 (1988).

495

Methods

Mechanical setup

The frame for our robotic system consists of a 1.5 m x 1 m rectangular framing system constructed from aluminum extrusions (OpenBuilds V-Slot 20 x 20 mm, 20 x 40 mm, and C-Beam 40 x 80 mm).

WormPicker's optical system and picking arm are moved by a motorized stage along 3 axes: X (1 m long), Y (1.5 m long), and Z (0.3 m long), In addition, there is a linear carriage under the plate tray that moves the illumination and plate tracking system. All axes are driven by stepper motors. For the X and Y axes, motors mounted to the carriage drive motion via a belt attached to both ends of the rail. For the Z axis, a stepper motor drives motion through rotation of a lead screw.

The maximum speed for the X axis was set to 146.67 mm/s, Y axis 146.67 mm/s, and Z axis 8.33 mm/s. The maximum acceleration for the X axis was set to 120 mm/s^2, Y axis 120 mm/s^2, and Z axis 10 mm/s^2. Stepper motors' motions are controlled through a PC via an OpenBuilds BlackBox motion control system using GRBL firmware.

All aspects of the robotic system were controlled by an Origin PC with an Intel(R) Core i9-10900K CPU at 3.7 GHz and 64 GB of RAM, running Windows 10.

Plate tray platform

We constructed a plate tray platform for housing an array of agar plates. The platform holds eight slide-in trays (Supplementary Fig. 2a), each of which is made of two laser-cut transparent acrylic boards (upper layer 3 mm thick, lower layer 4.5 mm thick) sandwiching a 16.26 μm-thick aluminum foil layer (Supplementary Fig. 2b). The function of the foil layer is to increase the capacitance change detected by the capacitive touch sensing circuit (Supplementary Fig. 3g) when the picking arm contacts the agar surface. Each tray is held by the framing rails, enabling the user to remove or replace the plate trays by sliding in and out (Supplementary Fig. 2a). Each plate tray is locked into place by a turn latch (McMaster, 1579N12). Coordinates of individual wells on the platform are calibrated and stored in a configuration file.

Plate tracking system

We developed methods for tracking agar plates throughout the experiment. A printed adhesive label containing a machine-readable barcode and human-readable text (Supplementary Fig. 2c) was attached to the side of each agar plate.

We designed the barcode label to contain 24 black bars, each representing one bit by its thickness (Supplementary Fig. 2c): a thick bar encodes 1, and a thin one 0. The thickness of each white space between the bits is the opposite of that of the bar to its left, such that every bit has the same length. Starting from the left, the first 20

bits encode the barcode's number as a 20-bit positive binary integer; the next 3 bars encode the MOD-8 checksum of the number, used by the algorithm to verify its decoding result. The final bar is always thin, and it functions as a checkpoint as the algorithm searches for its presence and stops decoding when the 24th bar is found.

We built a machine vision system for imaging and reading the barcode from beneath the plate tray (Supplementary Fig. 2d). A camera acquires label images through two lenses, and two LEDs provide uniform illumination onto the label (Supplementary Fig. 2e-f).

We developed machine vision algorithms (Supplementary Fig. 2g-i) for reading the barcode identifier. We train a barcode-finding Mask Regional Convolutional Neural Network[26] (BcMRC) for identifying the barcode in the image. We curated a training dataset containing 520 648-pixel x 486-pixel images, in which the contours of individual barcodes were manually labeled. The BcMRC was adapted from a pretrained ResNet-50-FPN[26] backbone, and imported through the PyTorch library. The training was performed with a Stochastic Gradient Descent (SGD) optimizer at a CPU (i7-10750H) and the model converged after 9 epochs. The model generates contour segmentation for the object most likely to be the barcode in the image (Supplementary Fig. 2g) (we assume there is only one barcode visible in the image). The mean Intersection over Union (IoU) score of the mask prediction and the ground truth is 0.942 (N = 120).

The BcMRC-predicted mask is split into 10 bins in the horizontal direction, and a scanning line is generated by connecting the centroids of each bin (Supplementary Fig. 2g). For each point on the scanning line, intensities of pixels lying in 10% FOV height upper and lower than the point are averaged for calculating the local intensity. From the left to right, the local intensity can be plotted along the scanning line (Supplementary Fig. 2h). Then, the local intensity profile is binarized by a threshold $H = (p_{0.1} + p_{0.9})/2$ (Supplementary Fig. 2i), where $p_{0.1}$ and $p_{0.9}$ are the 10 and 90 percentile values of the intensity profile. After thresholding, a bit is decoded as "1" if the width of the black portion is larger than its complementary white portion right next to it, otherwise, "0". The 20-bit number and the 3-bit checksum (red and blue in Supplementary Fig. 2i) are then converted from binary to decimal to obtain the unique identification number associated with the plate of interest T and its checksum C. If the checksum test passes, i.e., $T \bmod 8 = C$, then the barcode is decoded successfully; otherwise, an error is reported.

We constructed a database for cataloging a set of plates throughout the experiments (Methods). Information of individual plates can be looked up from the database through their unique identifiers. The database stores the key information including but not necessarily limited to the positions on the tray, strain names, genotypes, phenotypes, and histories. The database is arranged in a human- and machine-readable .csv format.

577 ## Dual-magnification multimodal optical imaging system

578 To implement bright-field imaging we constructed an illumination system under
579 the platform, in which light from a white LED is diffused by a ground glass and
580 collimated by a Fresnel condenser lens (Supplementary Fig. 3a). The low and high-
581 magnification imaging paths share a single objective lens (achromatic doublet, focal
582 length 100 mm). Light from the plate is collected by the main objective, then divided
583 into the low and the high magnification imaging streams by a beamsplitter (ratio of
584 transmission : reflection is 90% : 10%). The low-magnification image is relayed to a
585 machine vision camera by a camera lens, while the high-magnification image is
586 formed at a CMOS camera through a set of teleconverter lenses and a tube lens.
587 The high-magnification pathway is an infinity-corrected microscopy system that can
588 support both bright-field and fluorescence imaging.

589 For fluorescence imaging (Supplementary Fig. 3b-c), two collimated excitation
590 LEDs (center wavelengths 470 nm and 565 nm) and a set of dual-band fluorescence
591 optics (Chroma 59022) are built in the infinity space in the high-magnification
592 pathway. The spectra of the fluorescence optics were selected to enable both GFP
593 and RFP imaging.

594 Switching between the imaging modes can be achieved by digital relay circuits
595 controlling the excitation LEDs and the under-platform illumination (Supplementary
596 Fig. 3a-c, Supplementary Video 1). The specifications of the optics used in the
597 imaging system are listed in Supplementary Table 1.

Imaging focus control

The distance between the main objective lens and the agar surface is monitored by a custom-built laser-based level monitor (Fig. 1a, Supplementary Fig. 3d). A 532 nm laser containing a cylindrical lens generates a line lying in the y axis that is focused by a lens and projected onto the agar surface at an oblique angle (Supplementary Fig. 3d). Then, the distance between the objective lens and the agar surface then can be monitored by the position of the laser line observed by the imaging system. The 3D motorized stage brings the objective to the correct position, at which the agar surface lines up with its focal plane, by aligning the observed laser line to a previously calibrated position.

Lid handler

Lids are manipulated by two custom-built vacuum handlers mounted to the carriage of the 3D motorized stage (Fig. 1a, Supplementary Fig. 3e). Each handler consists of two 3D-printed sliding sockets holding a silicone tube, motorized by a micro linear actuator (Actuonix, PQ12-30-12-S). A tube fitting is attached to the end of the vacuum line. The height of the vacuum interface is controlled by the linear actuator and the vacuum is switched on or off by a solenoid valve (GRANZOW, H2U29-00Y).

To remove a lid, the main moving gantry positions the vacuum interface above the lid, the solenoid valve activates the vacuum, the linear actuator lowers the vacuum holder, the lid becomes attached by suction to the holder, and the linear

619 actuator raises the holder and the lid (Supplementary Video 2). To restore a lid, this
620 process is reversed.

621 **Robotic picking arm**

622 We custom-built a robotic arm (Supplementary Fig. 3f) for manipulating *C.*
623 *elegans* on agar media using a wire loop. The robotic picking assembly consists of a
624 linear stepper actuator, three stepper servo motors, and a custom-designed 3D-
625 printed worm pick (Fig. 1c). The linear stepper actuator fine tunes the z height of
626 the picking arm through a linear carriage. The stepper servo motors are chained
627 orthogonally to provide 3 degrees of freedom in rotation, i.e., θ, ω, φ (Fig. 1a), for the
628 worm pick. The 3D-printed worm pick is mounted to the Servo S1. The design allows
629 two copper wires to fit into the pick stem from the proximal end, and these two wires
630 are connected by a portion of looped platinum wire (90% Pt, 10% Ir, 254 μm
631 diameter) at the distal end of the pick (Fig. 1c). The platinum wire is crimped to
632 copper contact pins for attaching to the end of the pick.

633 To sterilize the pick, the platinum wire loop is connected to the heating power
634 supply (5V DC) by closing Relay 1 and 2, which is controlled by a LabJack
635 (Supplementary Fig. 3g). The resulting 4.5 A DC current sent through the wire
636 heats the loop to a temperature we estimate to exceed 1,000 ºC (Fig. 1c,
637 Supplementary Video 3).

638 We used the wire loop as a capacitive touch sensor (Supplementary Fig. 3g) to
639 monitor contact between the wire and the agar surface and provide feedback for

picking trajectories. For capacitive touch sensing, the platinum wire loop is first cut off from the heating circuit by opening Relay 2 (disconnecting the wire loop from the heating wires is essential for the capacitive touch sensing to function properly). The capacitive change due to the contact between the wire loop and the agar surface is sensed by a capacitive touch sensor chip. The capacitive touch sensor is powered by the LabJack, which also monitors its voltage output.

Pick focus control

For centering the pick tip to the high-magnification FOV, the user specifies the coordinates of the target point (x_f, y_f) in the low-magnification images to the system, and the system moves the pick tip to this position for the pick tip to be visible in the high-magnification FOV (see Methods for pick tracking). For estimating the z height for the pick tip to be in optimal focus in the high-magnification pathway, the system monitors the mean intensity of the top 20% darkest pixels $\overline{I_{20}}$ of the high-magnification image as a measure of focus (Supplementary Fig. 4). The system sets the z height z_f at which the $\overline{I_{20}}$ is minimized as the pick tip focus height. The system records the positions read out from the linear stepper actuator and the three servos, i.e., $(l_f, s_{f1}, s_{f2}, s_{f3})$, when the pick tip is at the focus position (x_f, y_f, z_f).

To pick a worm, the system positions the pick tip right above the remembered focus position, i.e., $(x_f, y_f, z_f - \Delta z)$, where Δz is a predefined small amount of height offset (approximately 2 mm). We set the position $(x_f, y_f, z_f - \Delta z)$ to be the initial position (IP in Fig. 1d and e), prior to carefully lowering the pick until touching the agar (Phase A in Fig. 1d and e).

We measured the precision of moving the pick tip to the remembered focus position in x and y axes. The mean deviation between the target focus position and the actual position of the pick tip is 290 μm (SD = 161 μm) in x and 250 μm with (SD = 173 μm) in y (N = 342). This precision allows the system to move the pick tip to the focus position directly by setting the $(l_f, s_{f1}, s_{f2}, s_{f3})$ to the linear actuator and the servos, without any closed-feedback-loop centering procedures, improving the worm picking speed.

Pick motion trajectories for manipulating *C. elegans*

To pick up a worm (Fig. 1d), the wire pick is positioned above the agar, with a y-offset to the target worm (IP). The linear stepper actuator vertically lowers (phase A, change in z) the pick until contacting the agar surface (TP) as perceived by the capacitive touch sensor. Next, Servo 2 horizontally swipes (phase B, change in ω) the pick on the agar surface in $+y$. Next, Servo 1 and 3 act simultaneously to perform a curved motion (phase C, change in θ and φ) for picking up the target animal using the outer side of the wire loop (FP). During phases A-C, the motor speeds are maximized.

To put down the worm to the substrate (Fig. 1e), the pick is positioned above the substrate (IP). The linear stepper actuator vertically lowers (phase A, change in z) the pick until touching (TP), monitored by the capacitive touch sensor. Next, Servo 2 horizontally swipes (phase B, change in ω) the pick on the agar surface in $-y$, during which the worm detaches from the wire in $+y$; for some cases the worm stick to the inner side of the wire loop, the moving stage swipes (phase C, change in x)

684 the pick in $-x$. Finally, Servo 1 vertically raises (phase D, change in φ) the pick
685 from the substrate (FP). Motor speed is tuned down to lower levels for different
686 phases, and waiting times were added between transitions between phases.

687 Parameters for the pick motion trajectories are listed in Supplementary Table 2,
688 with the sign convention depicted in Fig. 1a.

689 Machine vision

690 *C. elegans tracking in the low-magnification imaging stream*

691 We used a combination of machine learning and motion detection for tracking *C.*
692 *elegans* over the plate in the low-magnification imaging stream.

693 We trained WormCNN, a convolutional neural network (CNN) for making a
694 binary prediction of whether a 20-pixel x 20-pixel region of interest (ROI) contains
695 one or more worms. The structure of the WormCNN is depicted in Supplementary
696 Fig. 5a. We curated a training dataset containing 43,568 training images, 50%
697 worms, and 50% backgrounds (Supplementary Fig. 5b). With a batch size of 24 and
698 an SGD optimizer (momentum = 0.9), the model converged after 10 epochs. The
699 accuracy of the network is 97.23% on 10,784 test images (balanced test set, i.e.,
700 half worms and half backgrounds). The trained network was saved as a .onnx file,
701 which is imported to the system control software through the OpenCV DNN module.

702 In addition to the results from machine learning, we integrated motion
703 information for identifying worms over the plate. For a 20-pixel x 20-pixel ROI, we
704 constructed a simple motion detector by taking two frames Δt seconds apart,

subtracting the pixel values, and summing up the pixel differences Δp within the ROI. If the Δp is higher than a threshold p_h, i.e., $\Delta p > p_h$, then is it highly likely that the ROI contains worms. To determine the threshold, the automated system measured the pixel change for a group of animals (Mixed stages, N > 150) in its individual ROI in the past Δt seconds $(p_1, p_2, p_3, \dots, p_N)$, and we set the threshold as the mean value of the observation, i.e., $p_h = \frac{\sum_1^N p_N}{N}$.

We programmed the machine vision for *C. elegans* tracking functioning in two modes: Finding mode and Tracking mode. With the purpose of rapidly identifying worms over the agar plate, the Finding mode functions in a two-step manner: first it runs the motion detector over the entire image, then feeds the 20-pixel x 20-pixel ROI of the spots with movement detected, i.e., $\Delta p > p_h$ to the WormCNN, which generates a binary decision to indicate whether any animals present in the ROI. The coordinates of the ROI passing the criteria above are set to be the coordinates of the worms identified.

In contrast to the Finding mode that relies on both motion detection and machine learning, the Tracking mode is able to track the worms solely using the WormCNN, supplemented by subpixel processing. For a worm having a known coordinate $C_{n-1} = (X_{n-1}, Y_{n-1})$ in the image for the frame $n-1$, the Tracking mode updates the worm coordinate in the frame n by a few steps.

First, it constructs an 80-pixel x 80-pixel rectangular tracking region, centering at C_{n-1}. Second, it splits the tracking region image into multiple 20-pixel x 20-pixel ROIs

separated by a constant step size in x and y direction, and each of those is fed to the WormCNN to generate a confidence score wcs for each ROI. The confidence score is the output of the final fully connected layer of the WormCNN, indicating the likelihood of the input ROI containing any worms. Third, it calculates the centroid of the wcs for all the WormCNN ROIs in the tracking region, and sets it to be the worm coordinate in the frame n, i.e., $C_n = (X_n, Y_n)$. Assuming that there are a total number of m WormCNN ROIs in the tracking region, X_n and Y_n are obtained by

$$X_n = \frac{1}{WCS}\sum_{i=1}^{m} wcs_i x_i \; ; \; Y_n = \frac{1}{WCS}\sum_{i=1}^{m} wcs_i y_i$$

where wcs_i, x_i, and y_i are the confidence score, x, and y coordinates of centroid of the i-th WormCNN ROI, $WCS = \sum_{i=1}^{m} wcs_i$, the total confidence score of all the WormCNN ROIs.

The worm tracking region centers at $C_{n-1} = (X_{n-1}, Y_{n-1})$ and the WormCNN ROIs are constructed from the tracking region; this means x_i, and y_i are dependent on the coordinate of the worm in the frame $n-1$, i.e., C_{n-1}, the last known coordinate of the worm being tracked. Therefore, x_i and y_i can be written as $x_{n-1,i}$ and $y_{n-1,i}$ for indicating the temporal dependency. In short, the Tracking mode updates the coordinates of worms (X_n, Y_n) in the current image by the last seen coordinates (X_{n-1}, Y_{n-1}) by

$$(X_n, Y_n) = \left(\frac{1}{WCS}\sum_{i=1}^{m} wcs_i x_{n-1,i}, \frac{1}{WCS}\sum_{i=1}^{m} wcs_i y_{n-1,i}\right)$$

Using a combination of the Finding and Tracking mode, WormPicker is able to rapidly identify and move induvial animals to some target points in the image, e.g., the high-magnification FOV, preparing for imaging and manipulation. This process involves a few steps.

First, the system runs the Finding mode to identify the coordinates of worms in the image, i.e., (X_w, Y_w). Then, the main gantry moves the image of the animal to the target point by translating by ΔX_g and ΔY_g in x and y direction, where ΔX_g and ΔY_g are calculated by

$$\Delta X_g = \frac{X_t - X_w}{dp/dG}; \Delta Y_g = \frac{Y_t - Y_w}{dp/dG}$$

Where X_t and Y_t are the initial x and y coordinates of the target point in the image, dp/dG the amount of the pixel shift corresponding to one unit movement in the main gantry. By making the gantry movement above, the worm is viewed in proximity to the target point.

The worm can be kept centered at the target point by running the Tracking mode while the gantry is continuously making small-step jogging motions in x and y. The movements of the jogging in x and y are given by

$$dX_g = \frac{X_t - X_{n,w}}{|X_t - X_{n,w}|} S; dY_g = \frac{Y_t - Y_{n,w}}{|Y_t - Y_{n,w}|} S$$

where $X_{n,w}$ and $Y_{n,w}$ are x and y coordinates of the worm in the current frame n, and S the predefined step size for the gantry jogging.

764 ***Pick wire loop tracking in the low-magnification imaging stream***

765 We applied machine learning for tracking the pick wire loop in the low-
766 magnification imaging stream. We trained PickCNN, a CNN for determining whether
767 a 20-pixel x 20-pixel ROI contains the pick tip. The backbone of the PickCNN is the
768 same as WormCNN (Supplementary Fig. 5a). We curated a training dataset
769 containing 872,550 images, 50% containing the pick tip and 50% the background
770 (Supplementary Fig. 5c). With an SGD optimizer, the model was trained on a GPU
771 (NVIDIA GeForce GTX 1660). The accuracy of the network is 99.36% on 50,400 test
772 images (balanced test set, i.e., half pick tips and half backgrounds).

773 We applied the PickCNN, supplemented with subpixel processing, to track the
774 pick tip in real time. A 640-pixel x 480-pixel (2 cm x 1.5 cm) rectangular region
775 centered at the low-magnification image is defined for tracking the pick tip inside that
776 region. This tracking region then is split into multiple 20-pixel x 20-pixel ROIs with a
777 constant skip step in x and y direction, each of those is fed to the PickCNN for
778 generating a confidence score pcs for each ROI. The confidence score pcs is the
779 output of the final fully connected layer of the PickCNN, indicating the likelihood of
780 the ROI containing the pick tip.

781 Assuming there is only one picking arm visible, among all the PickCNN ROIs,
782 the one with the highest pcs is considered the closest to the actual pick tip position.
783 By performing subpixel processing surrounding the ROI with the highest pcs and
784 the centroid coordinate of (x_h, y_h), the coordinate of the pick tip position (X_p, Y_p)
785 can be inferred by

$$(X_p, Y_p) = \left(\frac{1}{PCS}\sum_{i=1}^{n} pcs_i x_i, \frac{1}{PCS}\sum_{i=1}^{n} pcs_i y_i\right); \forall (x_i, y_i): \sqrt{(x_i - x_h)^2 + (y_i - y_h)^2} < r$$

where pcs_i, x_i, and y_i are the confidence score, x and y coordinates of the centroid of the i-th PickCNN ROI, $PCS = \sum_{i=1}^{n} pcs_i$, the total confidence score of the PickCNN ROIs. The equation above indicates that all the PickCNN ROIs having pixel distance to (x_h, y_h) less than a threshold r are taken into subpixel processing for determining the pick tip position (X_p, Y_p). We set the threshold $r = 60$ pixel (1.85 mm).

We measured the precision of tracking the pick tip in x and y axes. The mean deviation between the tracked position and the actual position of the pick tip is 94.9 μm (SD = 43.0 μm) in x and 284.5 μm (SD = 147.2 μm) in y (N = 225).

***C. elegans* segmentation in the high-magnification imaging stream**

We trained a Worm-finding Mask Regional Convolutional Neural Network[26] (WorMRC), for pixel-wise segmentation of individual animals in the high-magnification FOV. We curated a training dataset containing 2,697 images, each 612 x 512 pixels, over different developmental stages, ranging from L1 larvae to adults, in which the contours of individual animals were manually labeled. The WorMRC was adapted from a pretrained ResNet-50-FPN[26] backbone, and imported through the PyTorch library. With an SGD optimizer (momentum = 0.9), the model was trained at a GPU (NVIDIA GeForce GTX 1660 Ti) and converged after 10 epochs. The model outputs bounding boxes for the objects that are likely to be worms and generates contour segmentation for the object within each bounding box.

807 WorMRC robustly segments individual animals over complex backgrounds
808 (Supplementary Fig. 5d). Contour areas of individual animals (of mixed stages, L1 –
809 Adults) segmented by WorMRC verse manual segmentation gold standard are
810 plotted in Supplementary Fig. 5e. The areas of WorMRC predicted worm contours
811 present high consistency with the ground truth, R^2 = 0.972 (N = 690).

812 ***Developmental stage determination***

813 The developmental stages of the animals in the high-magnification images are
814 inferred by their lengths. The centerline of the individual worm contour can be
815 obtained by the methods previously reported[50]. We obtained the lengths for different
816 developmental stages from the literature[51] and obtained the decision boundaries for
817 approximately identifying developmental stages: L1s are < 370 μm, L2s 370 – 500
818 μm, L3s 500 – 635 μm, L4s 635 – 920 μm, adults > 920 μm.

819 ***Morphological analysis***

820 To perform the genetic cross between the *dpy-5* mutant and *dop-1p::GFP*
821 transgenic (Fig. 3) we developed an algorithm for assaying the Dumpy (Dpy)
822 phenotype. The *dpy-5* mutant displays shorter and stouter morphology than control
823 animals. We measured the aspect ratio AR of the animal, $AR = \frac{A}{L^2}$, where A is the
824 area of the contour segmented by the WorMRC and L the length of the centerline of
825 the worm contour[50]. We used the automated system to acquire images of *dpy-5*
826 mutants (CB61) and wild-type animals (N2) (N = 190).

827 Based on this dataset, we determined a AR threshold for identifying Dpy
828 animals for unseen worms. ARs of individual Dpy and wild-type animals are plotted
829 in Supplementary Fig. 5f. With an 80-20 train-test split, we constructed a one-
830 dimensional support vector machine (SVM) to classify Dpy and wild-type phenotypes
831 based on the AR. The SVM-generated decision boundary gives 100% accuracy on
832 both the training and the test sets (Supplementary Fig. 5f). We recorded this
833 threshold to classify future samples: if a worm has an AR greater than the threshold,
834 then the worm is classified as Dpy; otherwise it is classified as having wild-type
835 morphology.

836 ***Sex determination***

837 *C. elegans* males and hermaphrodites display distinct tail morphologies, with a
838 fan structure visible in the tails of males. We trained a sex-determining Mask
839 Regional Convolutional Neural Network[26] (SexMRC), for determining the sexes of *C.*
840 *elegans* based on the high-magnification images. We curated a training dataset
841 containing 6,860 images (612 x 512 pixels), in which contours of heads, tails for
842 hermaphrodites, and tails for males, were manually labeled. The SexMRC was
843 adapted from a pretrained ResNet-50-FPN[26] backbone, and imported through the
844 PyTorch library. The model was trained with an SGD optimizer (momentum = 0.9) at
845 a GPU (NVIDIA GeForce GTX 1660 Ti) and the model converged after 7 epochs.
846 The model outputs bounding boxes for the objects that are likely to be *C. elegans*
847 heads, tails for hermaphrodites, and males, as shown in Supplementary Fig. 5g. The
848 network identifies males with 100% precision and 85.71% sensitivity (recall) and

identifies hermaphrodites with 92.45% precision and 92.45% sensitivity (recall) (N = 74).

Embryo detection

We trained an Embryo-finding Mask Regional Convolutional Neural Network[26] (EmbMRC), for identifying embryos in the high-magnification images. We curated a training dataset containing 454 images (612 x 512 pixels), in which the contours of unhatched embryos were manually labeled. The EmbMRC was adapted from a pretrained ResNet-50-FPN[26] backbone, and imported through the PyTorch library. The network was trained with an SGD optimizer, at a GPU (NVIDIA GeForce GTX 1660 SUPER) and the model converged after 10 epochs. The model outputs bounding boxes for the objects that are likely to be embryos and generates contour segmentation for the objects within each bounding box (Supplementary Fig. 5h). Supplementary Fig. 5h shows the image overlayed with EmbMRC segmentations when a few, a medium number of, and a larger number of embryos present in the FOV. The numbers of embryos counted by EmbMRC are highly consistent with results from manual counting ($R^2 = 0.9772$, N = 124) (Supplementary Fig. 5i).

Fluorescence phenotyping

Using the multimodal imaging system (Supplementary Fig. 3a-c), the automated system is able to observe different fluorescent markers expressed in *C. elegans*. The genetic experiments we presented in this study require determining whether the individual animals carry fluorescent markers.

870 To do this, the automated system moves to view individual worms in the high-
871 magnification FOV and captures one bright field and one fluorescence frame,
872 between which the elapsed time is ~250 ms. The bright field frame is then delivered
873 to the WorMRC for obtaining the contour segmentations for the individual worms
874 found in the high-magnification FOV; while the fluorescent frame is binarized by a
875 threshold h_i, and the bright spots obtained after the thresholding are filtered
876 according to their sizes, for reducing noise. The bright spots with sizes larger than a
877 threshold h_s are kept as true fluorescent spots; otherwise, they are discarded. Both
878 h_i and h_s were manually calibrated on the strains of interest, and they can vary
879 across different strains and imaging conditions. For each worm identified in the
880 bright-field image, we dilate the contour mask to compensate the potential mismatch
881 between the bright-field and fluorescent frames due to the worms' free-roaming
882 behaviors during the acquisition elapsed time, i.e. the ~250 ms. The animals cut off
883 by the FOV boundaries were filtered out for fluorescence phenotyping, preventing
884 false negatives.

885 For a moderately bright fluorescent transgenic strain (LX811, Fig. 4a), the
886 algorithm classifies fluorescence phenotypes for individual worms of mixed stages
887 with an accuracy of 97.16% (N = 211). Imaging and processing parameters for
888 fluorescence phenotyping for different experiments are listed in Supplementary
889 Table 3.

890 ***Intermediate picking***

891 Depending on the application, the automated system may be required to
892 precisely transfer a single animal with some desired phenotypes and stray animals
893 are strictly prohibited, for example, isolating F2s for identifying a transgenic integrant
894 (Fig. 5). For those experiments, we programmed the automated system to perform
895 intermediate picking if multiple worms or/and unhatched embryos founded in the
896 high-magnification FOV by the WorMRC or/and EmbMRC. The system first inspects
897 all the animals in the high-magnification image, if none of them carries desired
898 phenotypes, the system inspects other animals; if at least one carries the desired
899 phenotypes, the robotic arm picks up the target animal, possibly along with
900 surrounding ones. Then, the system puts the animals down onto a fresh intermediate
901 plate and waits a few seconds allowing the worms to move. The system then picks
902 up the single worm with the desired phenotypes.

903 ***Verification of the transfer results***

904 Verifying whether the animal was successfully transferred to the destination plate
905 is done via a two-step strategy. First, the automated system attempts to put down
906 the worm in the high-magnification FOV, and it observes whether any worms can be
907 found in the FOV using the WorMRC. If so, the transfer is deemed as a success,
908 otherwise continuing with the next step. Second, it observes whether any animals
909 crawling out from the proximity of the spot where the worm was put down in the low-
910 magnification FOV. If there are any such animals, the operation is deemed a
911 success.

Using human observation as the gold standard the verification strategy has 97.22% accuracy for verifying the results of transfer attempts (N = 108); the transfer success rate is 94.83% (N = 58).

WormPickerControl and WormPickerLib

For WormPicker to perform useful work, the basic elements of identifying and transferring worms need to be combined to form multi-step genetics procedures. For this purpose, we developed system control software, WormPickerControl (Supplementary Fig. 7a). This software is written in Python for the frontend and C++ for the backend. The frontend is an Application Programming Interface (API), enabling the user to write scripts for specifying tasks to be performed by the automated system. We developed utilities in the API for initiating resources, generating scripts, managing a set of scripts, and supplementing the API to send the script commands to the C++ backend.

To further improve speed, we set up multiple threads in the C++ backend for separately handling image acquisition, image processing, hardware control, and script execution. We developed a library of source scripts, WormPickerLib, in the C++ backend, executing each of which enables the hardware to perform specific tasks. The user has full access to WormPickerLib through the Python API, by which the user has the flexibility to combine a set of scripts for generating custom protocols.

We bridged up channels connecting the Python API, WormPickerLib, and the hardware for script execution management and data transfer.

We constructed a database, storing information in .csv format, through which the automated system is able to catalog a set of plates throughout the experiments. The API and WormPickerLib interact with the database, i.e., data reading and writing.

We constructed a Mask-RCNN segmentation server, written in Python, responsible for making Mask-RCNN inferences on the images acquired from different cameras. The segmentation server loads the multiple Mask-RCNN models from the saved .pth files, including WorMRC, SexMRC, EmbMRC, and BcMRC. We built client-server sockets connecting WormPickerLib to the Python segmentation server, through which images acquired by the C++-controlled hardware are sent to the corresponding Mask-RCNN models, and the inference results are sent back to the software for subsequent processing (Supplementary Fig. 7a).

WormPickerLib contains commands for performing a set of common *C. elegans* genetics procedures, which are categorized into low-, mid-, and high-level scripts. Elements in the library, along with their names and descriptions are tabulated in Supplementary Table 4. We arranged the call stack architecture in a hierarchy (Supplementary Fig. 7b).

The low-level scripts enable the system to execute individual basic actions, such as sterilizing the pick, finding a worm with some desired phenotypes, picking, and putting down the worm. The mid-level scripts are composed of multiple low-level

953 scripts chained in series, for example, picking multiple animals with some desired
954 phenotypes from a source to a destination. The high-level scripts are one iteration
955 above the mid-level scripts, enabling the system to carry out complete *C. elegans*
956 genetic procedures. The high-level scripts consist of a group of mid-level scripts
957 arranged in a timed and conditional manner. The user has the flexibility to develop
958 custom mid-level or high-level procedures using elements in WormPickerLib.

959 Taking the genetic mapping experiment (Fig. 4c) as an example, Supplementary
960 Fig. 7b depicts the representative scripts, along with their key input arguments, used
961 for generating a genetic cross between two strains JK2810 and LX811. The user
962 wrote high-level scripts, CrossWorms, SingleWorms. ScreenPlates, for instructing
963 WormPicker to set up the mating of P0, singling F1s, and screening F2s,
964 respectively (Fig. 4c). Execution of CrossWorms relied on calling the mid-level script
965 PickNWorms twice, each time for picking a certain number of males or
966 hermaphrodites to a plate for mating. Then, each time PickNWorms was executed
967 by iterating a set of low-level scripts, combining the set of basic actions of imaging
968 and manipulation.

969 **Strains**

970 We cultivated all the *C. elegans* strains used in this study in the dark at 20°C on
971 nematode growth medium (NGM) plates with OP50 bacteria using standard
972 methods[52]. The strains used are described in Supplementary Table 5. All
973 experiments were carried out at room temperature.

974 **Theory of the genetic mapping experiment**

975 Using the automated methods, we performed genetic mapping of an RFP
976 transgene *vsIs33 [dop-3p::RFP]* using classic genetics. The linkage of *vsIs33* to
977 different chromosomes is revealed by setting up genetic crosses between the strain
978 of interest (LX811) and a set of genetic balancers having *myo-2::GFP* markers.

979 The first genetic balancer strain we used was JK2810, carrying *hT2*[28] reciprocal
980 translocation in I and III, for determining linkage to I and III. As shown in
981 Supplementary Fig. 8, WormPicker crossed JK2810 males with LX811
982 hermaphrodites and picked out F1 cross-progeny that were both Red and Green.
983 According to the theory, the F2 self-progeny descending from these double-
984 fluorescent F1s would display a segregation pattern for the Red and Green, as
985 shown in the Punnett squares (Supplementary Fig. 8). If *vsIs33* is on neither I nor III,
986 the theory predicts 75% of non-Green animals would be Red, i.e., P (Red | non-
987 Green) = 0.75 (Supplementary Fig. 8a); while if *vsIs33* is on either I or III, 100% of
988 non-Green would be Red, i.e., P (Red | non-Green) = 1 (Supplementary Fig. 8b).

989 Using the same scheme, to determine linkage to other autosomes, the
990 automated system performed genetic crosses between LX811 and other GFP-
991 labeled genetic balancers, picked double-fluorescent F1 cross-progeny, and
992 screened for the segregation pattern of Red and Green in F2s. These balancer
993 strains include VC170, carrying *mIn1*[34] inversion in II (Supplementary Fig. 9),
994 CGC34, carrying *eT1*[29,30] reciprocal translocation in III and V (Supplementary Fig.
995 10), JK2958, carrying *nT1*[31-33] reciprocal translocation in IV and V (Supplementary

996 Fig. 11). For all the autosomal genetic balancers, the theory predicts 75% of non-
997 Green F2s would be Red if unsuccessfully balanced, and 100% if successfully
998 balanced.

999 Probing the linkage to the X chromosome requires a different scheme
1000 (Supplementary Fig. 12). WormPicker crossed wild-type males harboring a dominant
1001 extrachromosomal transgene *qnEx615[myo-2p::GFP]* (NQ1155) with LX811
1002 hermaphrodites, and picked out double-fluorescent F1 males, which were
1003 subsequently crossed with N2 (wild-type) hermaphrodites. The theory predicts none
1004 of F2 males would be Red if the transgene of interest is X-linked, and 50% if not X-
1005 linked.

1006 The patterns in F2s observed by the automated system, together with the linked
1007 and unlinked patterns in theory, are depicted in Supplementary Fig. 13a-b.

1008 For each autosomal linkage test described above, WormPicker screened over
1009 F2s and obtained the number of non-Green animals that were Red, N_{A1}, and non-
1010 Red, N_{A2}, and the total number of non-Green animals screened, $N = N_{A1} + N_{A2}$
1011 (Supplementary Fig. 13a). The red bars represent the observed percentages of Red
1012 among non-Green animals, $p_{A1} = \frac{N_{A1}}{N_{A1}+N_{A2}}$, while the gray bars the percentages of
1013 non-Red among non-Green animals, $p_{A2} = \frac{N_{A2}}{N_{A1}+N_{A2}}$. Each error bar indicates one
1014 standard deviation SD_A higher and lower than the observed percentage under the
1015 unlinked assumption, where $SD_A = \sqrt{\frac{p_{AUL}(1-p_{AUL})}{N}}, p_{AUL} = 0.75$.

Similarly, for testing X-linkage, the automated system screened over F2s and obtained the number of males that were Red, N_{X1}, and non-Red, N_{X2}, and the total number of males screened $N = N_{X1} + N_{X2}$ (Supplementary Fig. 13b). The red bar represents the observed percentage of Red among males, $p_{X1} = \frac{N_{X1}}{N_{X1}+N_{X2}}$, while the gray bar the percentage of non-Red among males, $p_{X2} = \frac{N_{X2}}{N_{X1}+N_{X2}}$. Each error bar indicates one standard deviation SD_X higher and lower than the observed percentage under the X-unlink assumption, where $SD_X = \sqrt{\frac{p_{XUL}(1-p_{XUL})}{N}}, p_{XUL} = 0.5$.

To quantify the linkage strength, we designed a quantity to measure the similarity between the link pattern in theory and the observed pattern and name it Linkage Index. Supplementary Fig. 13c shows the intuitive understanding of the Linkage Index.

To derive the Linkage Index, we first vectorize the link $\boldsymbol{W}_L$ and unlink $\boldsymbol{W}_{UL}$ patterns in theory and the observed pattern $\boldsymbol{W}_{obs}$ as following,

$$\boldsymbol{W}_L = \begin{bmatrix} p_L \\ 1 - p_L \end{bmatrix}, \boldsymbol{W}_{UL} = \begin{bmatrix} p_{UL} \\ 1 - p_{UL} \end{bmatrix}, \boldsymbol{W}_{obs} = \begin{bmatrix} N_1 \\ N_2 \end{bmatrix}$$

For the autosomal linkage test, p_L and p_{UL} are the percentage of non-Green animals that would be Red for the link and unlink pattern in theory, i.e., $p_L = 1, p_{UL} = 0.75$; N_1 and N_2 the observed count numbers of non-Green animals that were Red and non-Red. For the X linkage test, p_L and p_{UL} are the percentage of males that would be Red for the X-link and X-unlink pattern in theory, i.e., $p_L = 0, p_{UL} = 0.5$; N_1 and N_2 the observed count numbers of males that were Red and non-Red.

Let $\boldsymbol{e}_L$ and $\boldsymbol{e}_{UL}$ be the unit vectors pointing to the same direction as $\boldsymbol{W}_L$ and $\boldsymbol{W}_{UL}$, i.e.,

$$\boldsymbol{e}_L = \frac{\boldsymbol{W}_L}{\|\boldsymbol{W}_L\|}, \boldsymbol{e}_{UL} = \frac{\boldsymbol{W}_{UL}}{\|\boldsymbol{W}_{UL}\|}$$

($\|\ \ \|$ denotes the L2-norm of the vector). Then we set $\boldsymbol{e}_L$ and $\boldsymbol{e}_{UL}$ as basis vectors and $\boldsymbol{W}_{obs}$ can be expressed in terms of the basis

$$\boldsymbol{W}_{obs} = v_1\boldsymbol{e}_L + v_2\boldsymbol{e}_{UL} = [\boldsymbol{e}_L, \boldsymbol{e}_{UL}]\boldsymbol{v}_{obs}$$

where $\boldsymbol{v}_{obs} = \begin{bmatrix} v_1 \\ v_2 \end{bmatrix}$ is the coordinate of $\boldsymbol{W}_{obs}$ with respect to the basis $\boldsymbol{e}_L$ and $\boldsymbol{e}_{UL}$. $\boldsymbol{v}_{obs}$ can be obtained by

$$\boldsymbol{v}_{obs} = [\boldsymbol{e}_L, \boldsymbol{e}_{UL}]^{-1}\boldsymbol{W}_{obs}$$

where $[\ \ ]^{-1}$ denotes the inverse of the matrix. The coordinates of basis vectors themselves are $\boldsymbol{v}_L = [\boldsymbol{e}_L, \boldsymbol{e}_{UL}]^{-1}\boldsymbol{e}_L = \begin{bmatrix} 1 \\ 0 \end{bmatrix}$ for $\boldsymbol{e}_L$ and $\boldsymbol{v}_{UL} = [\boldsymbol{e}_L, \boldsymbol{e}_{UL}]^{-1}\boldsymbol{e}_{UL} = \begin{bmatrix} 0 \\ 1 \end{bmatrix}$ for $\boldsymbol{e}_{UL}$.

Next we define the Linkage Index $Lidx$ as the cosine similarity between the $\boldsymbol{v}_{obs}$ and $\boldsymbol{v}_L$:

$$Lidx = cos\ \theta = \frac{\langle \boldsymbol{v}_{obs}, \boldsymbol{v}_L \rangle}{\|\boldsymbol{v}_{obs}\| \cdot \|\boldsymbol{v}_L\|}$$

where θ is the angle formed by the $\boldsymbol{v}_{obs}$ and $\boldsymbol{v}_L$ (Supplementary Fig. 13c) and $\langle\ \ \rangle$ denotes the vector inner product. If the observed pattern is close to the link pattern, then $\theta \to 0$, yielding $Lidx \to 1$, implying a strong linkage to the chromosomes of interest. If on the other hand the observed pattern is similar to the unlink pattern, the $\theta \to 90°$, yielding $Lidx \to 0$, implying a weak linkage. Note that

1056 we cannot draw any conclusions when $Lidx \to -1$ because it suggests the

1057 observed pattern far deviated from both the link and unlink patterns in theory.

1058 The observed Linkage Indices for *vsIs33* over different chromosomes are shown

1059 in Supplementary Fig. 13d. We found that *vsIs33* displays strong linkage to either

1060 III or V and, to either IV or V, suggesting the transgene of interest is linked to V (Fig.

1061 4d).

Figures

Fig. 1 WormPicker system configuration

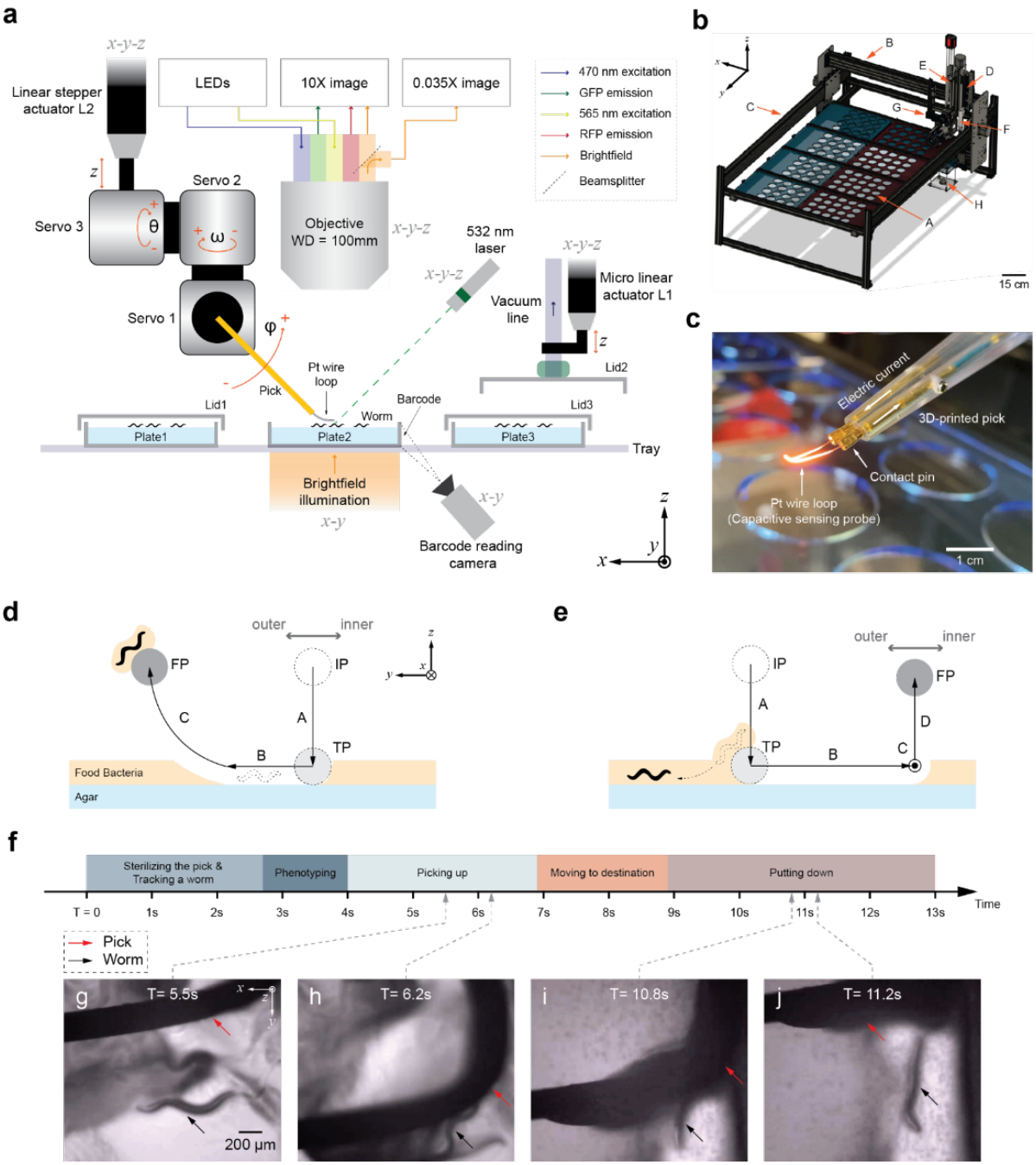

Fig. 1 | WormPicker system configuration. a, WormPicker geometry. *C. elegans* is manipulated by a wire pick motorized by servo motors and a linear stepper actuator. Animals are imaged by an optical imaging stream. Lids are manipulated by a vacuum grabbing system. The imaging and manipulation assemblies are mounted on a 3D motorized stage. **b**, WormPicker system overview. A:

plate tray platform; B-D: x, y, z linear rails for the motorized stage. E: optical imaging system; F: lid handler; G: robotic picking arm; H: LED illuminator. **c**, Photograph of the 3D-printed pick, captured when the wire loop being sterilized by an electric current. **d**, **e**, Schematic of pick motion trajectories for *C. elegans* picked up from and put down to agar substrate. TP: agar-touching position; FP: final position. **f**. Timeline for stages throughout the automated *C. elegans* transfer. **g-j**: key frames captured by the high-magnification camera during the Picking up (**g**, **h**) and Putting down stage (**i**, **j**).

Fig. 2 Overview of machine vision approaches

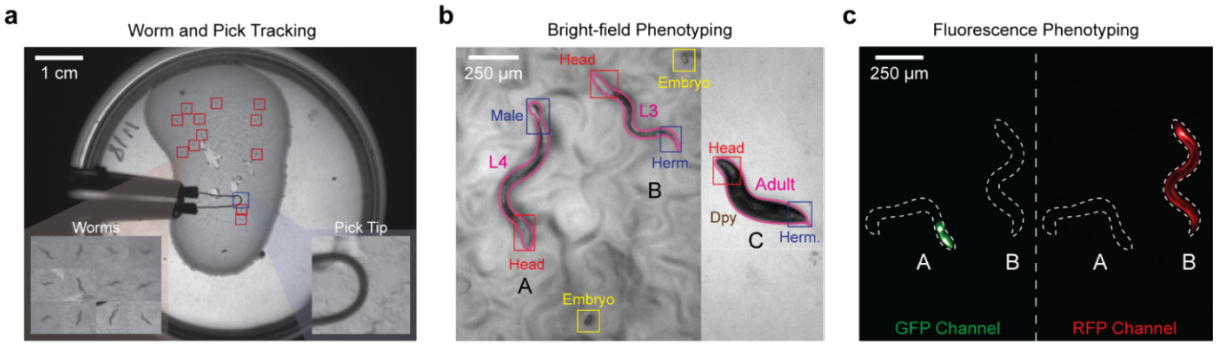

Fig. 2 | Overview of machine vision approaches. Machine vision algorithms for analyzing frames acquired from the low- (**a**) and high-magnification (**b**-**c**) imaging streams. The low-magnification frames (**a**) are analyzed for tracking worms and the pick in real time. The high-magnification bright-field images (**b**) are processed by a set of Mask-Regional CNNs (Mask-RCNNs) for close inspection on individual animals. Worms' contours are segmented by a Mask-RCNN (pink solid-line contours), and their developmental stages (including embryos), sexes, and morphological features can be assayed. The high-magnification fluorescent images (**c**) are subject to intensity analysis for identifying fluorescent markers in GFP and RFP channels. White dash-line: animal contours segmented in the bright field.

1087 **Fig. 3 Automated genetic cross in *C. elegans***

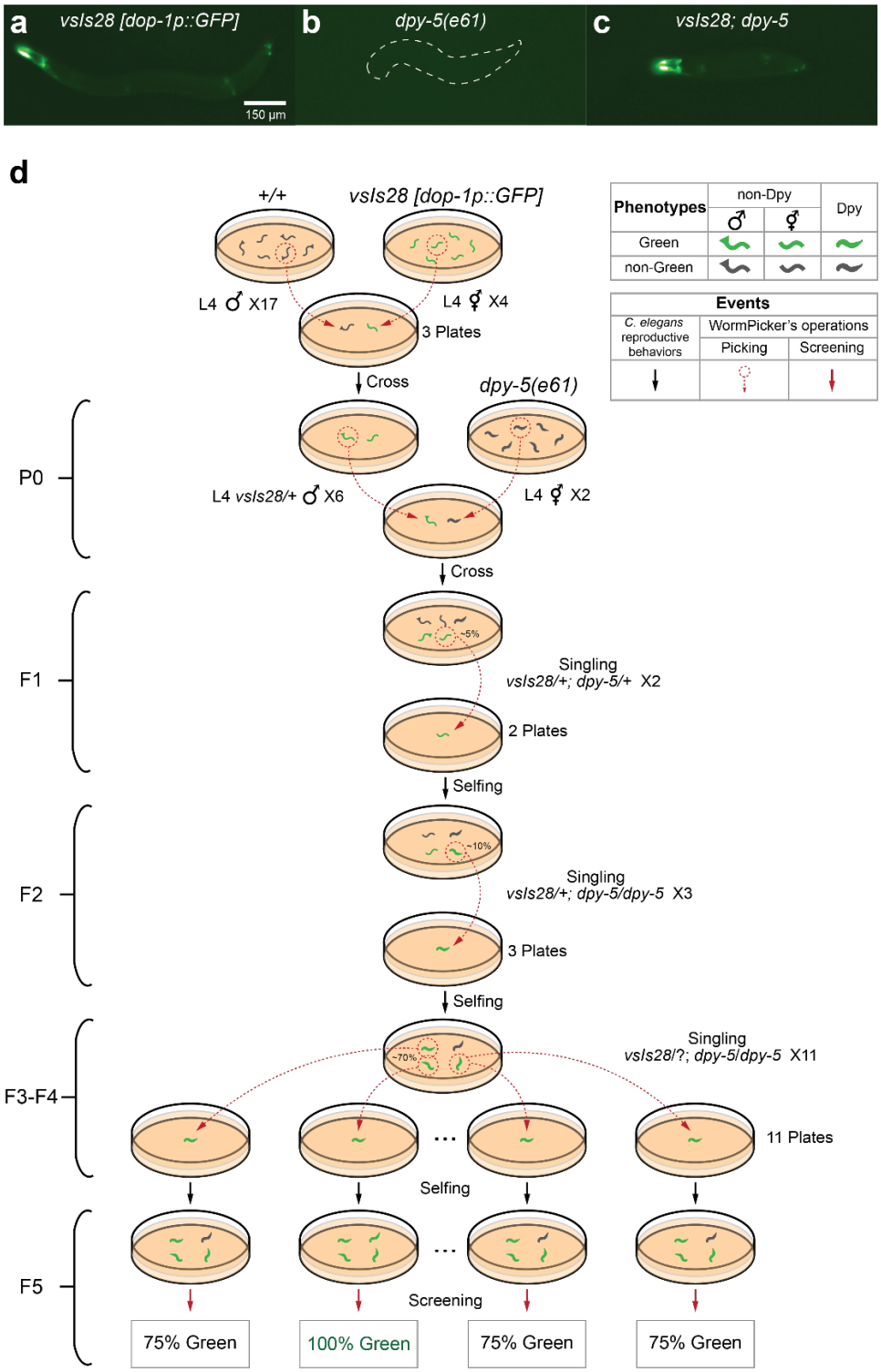

1088

1089 **Fig. 3 | Automated genetic cross in *C. elegans*.** WormPicker generated a genetic cross between

1090 animals carrying an integrated fluorescent transgene *vsIs28 [dop-1p::GFP]* and *dpy-5(e61)* mutants.

1091 **a-c**, GFP expression in the strain carrying *vsIs28* (**a**), *dpy-5* (**b,** worm contour marked by the white

dash line), and their hybridization *vsIs28*; *dpy-5* (**c**). **d**. Schematic of the genetic cross, with worms' phenotypes and events depicted by the legend.

Fig. 4 Automated genetic mapping of a transgene in *C. elegans*

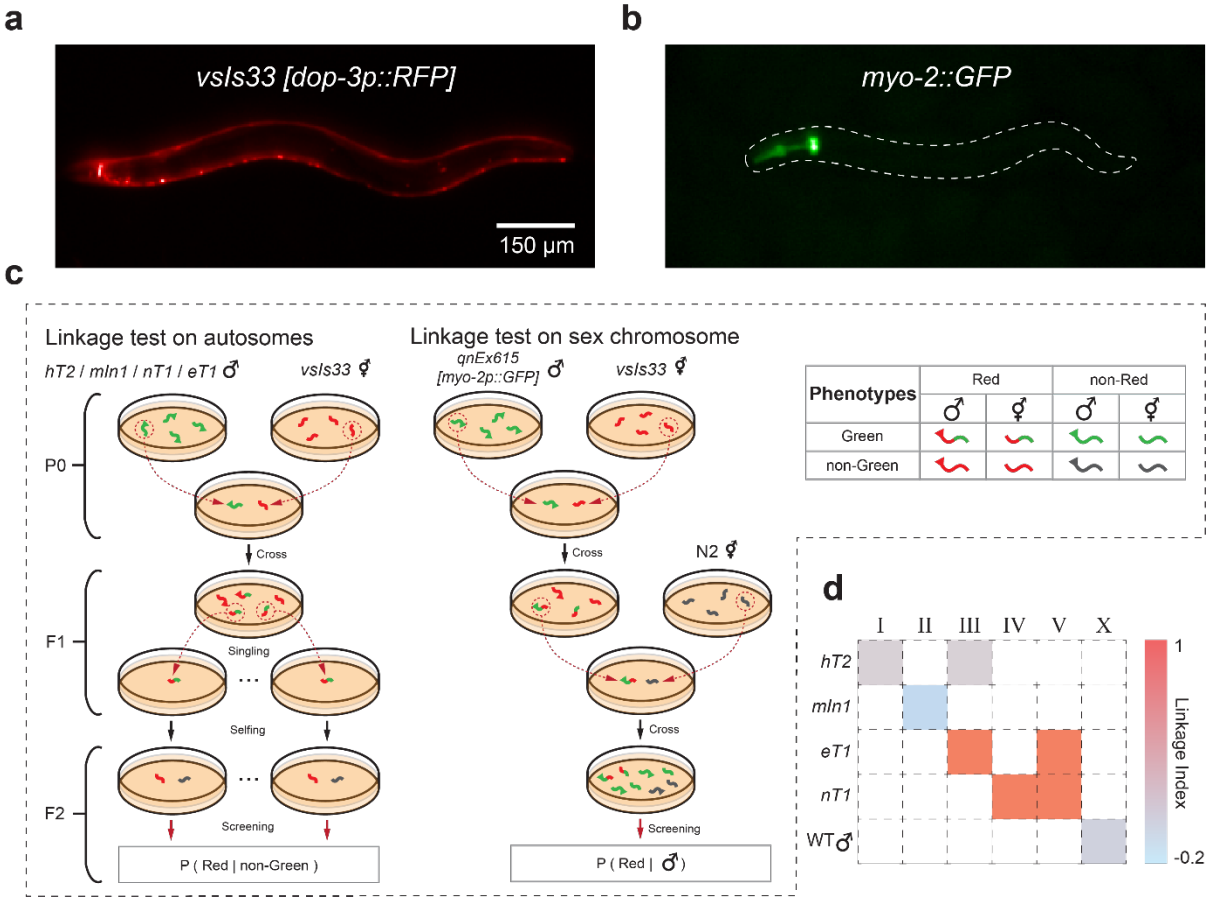

Fig. 4 | Automated genetic mapping of a transgene in *C. elegans*. WormPicker performed a genetic mapping of a red fluorescent transgene *vsIs33 [dop-3p::RFP]*. **a**. RFP expression in the transgenic strain carrying *vsIs33* (LX811). **b**. GFP expression in the *myo-2::GFP*-labeled genetic balancer strains. **c**. Schematic of linkage test on chromosomes with worms' phenotypes depicted by the legend and the event code same as Fig. 3d. **d**. Linkage of *vsIs33* over chromosomes, quantified by the Linkage Index in a heatmap. x axis: indices of the chromosomes; y axis: list of genetic balancers on distinct set of the chromosomes.

1103 **Fig. 5 Genomic integration of a transgene**

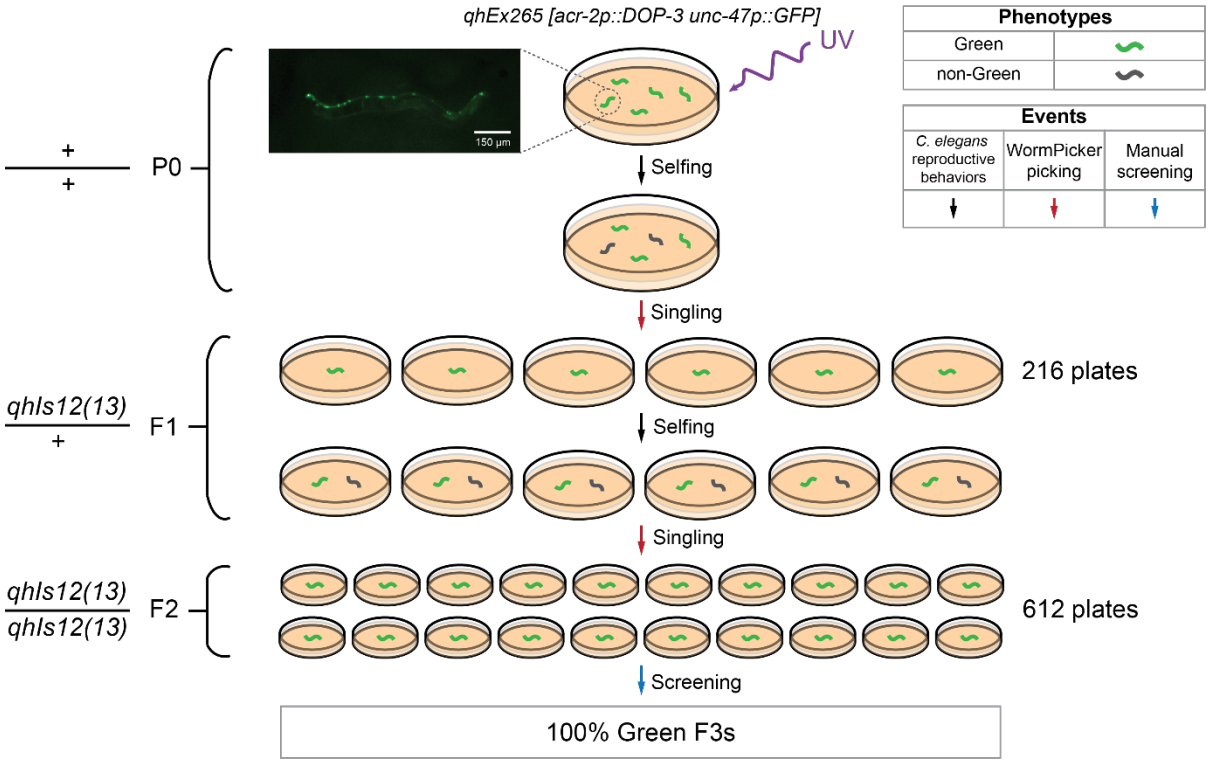

1104

1105 **Fig. 5 | Genomic integration of a transgene.** WormPicker automated a genomic integration of a

1106 *unc-47p::GFP*-labeled extrachromosomal array *qhEx265 [acr-2p::DOP-3 unc-47p::GFP]*. The image

1107 shows the GFP expression of the array of interest. The figure depicts the schematic of the transgene

1108 genomic integration with worms' phenotypes and events depicted in legend. WormPicker undertook

1109 all the picking tasks throughout the experiment. Finally, two integrated lines were manually identified,

1110 after which the transgenic alleles were given the names *qhIs12* and *qhIs13*.

Supplementary Information

Supplementary Fig. 1 WormPicker hardware architecture

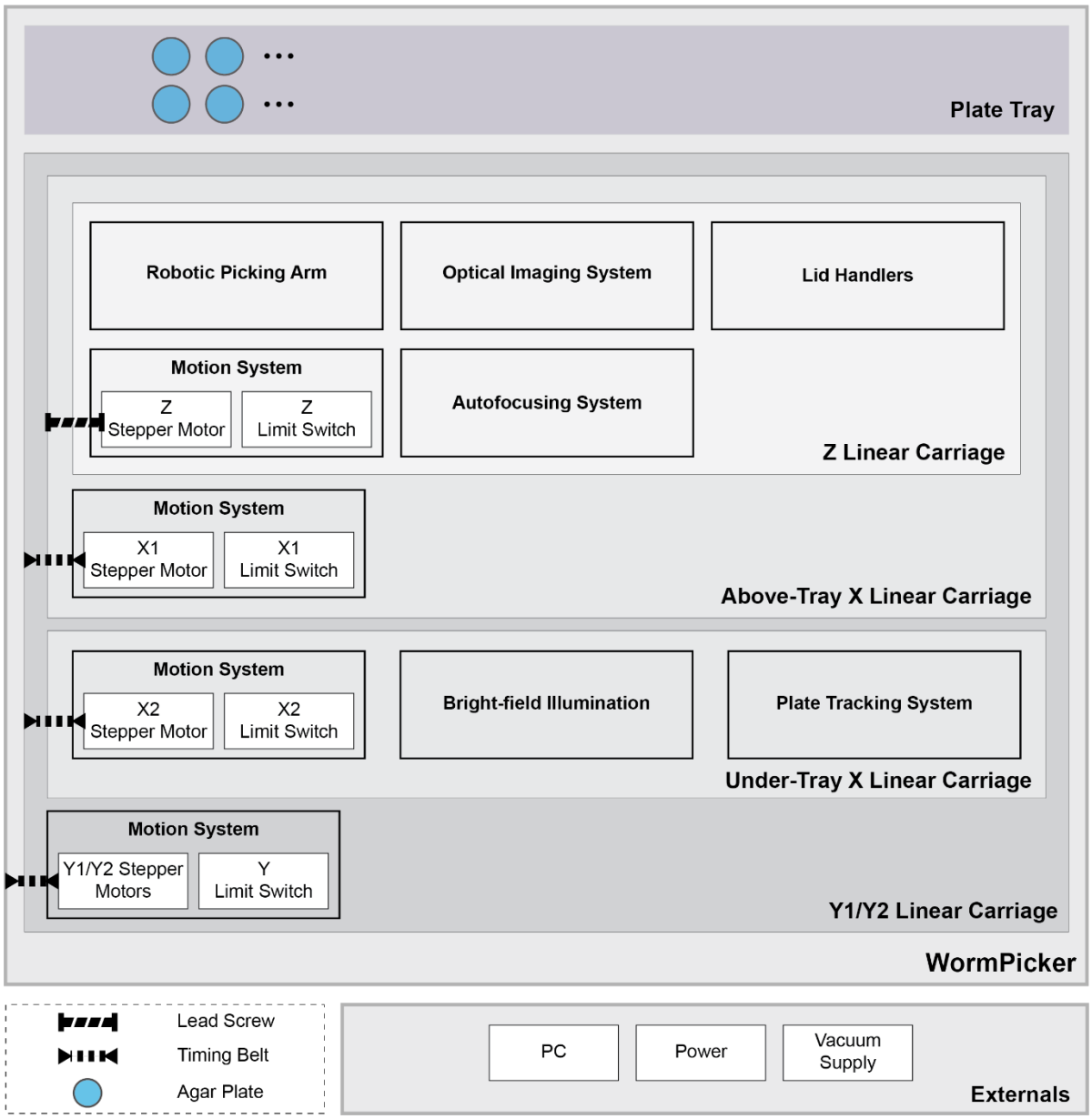

Supplementary Fig. 1 | WormPicker hardware architecture. WormPicker is composed of two modules, including a plate tray platform housing an array of agar substrates and linear carriage assemblies built in Cartesian coordinates, i.e., X, Y, and Z. The Z linear carriage motorizes animal imaging and manipulation assemblies, including a robotic picking arm, an optical imaging system, two lid handlers, and an Auto-image focuser. The under-tray X linear carriage motorizes supplementary

1119 tools, including bright-field illumination and plate tracking module.

Supplementary Fig. 2 Plate tray platform

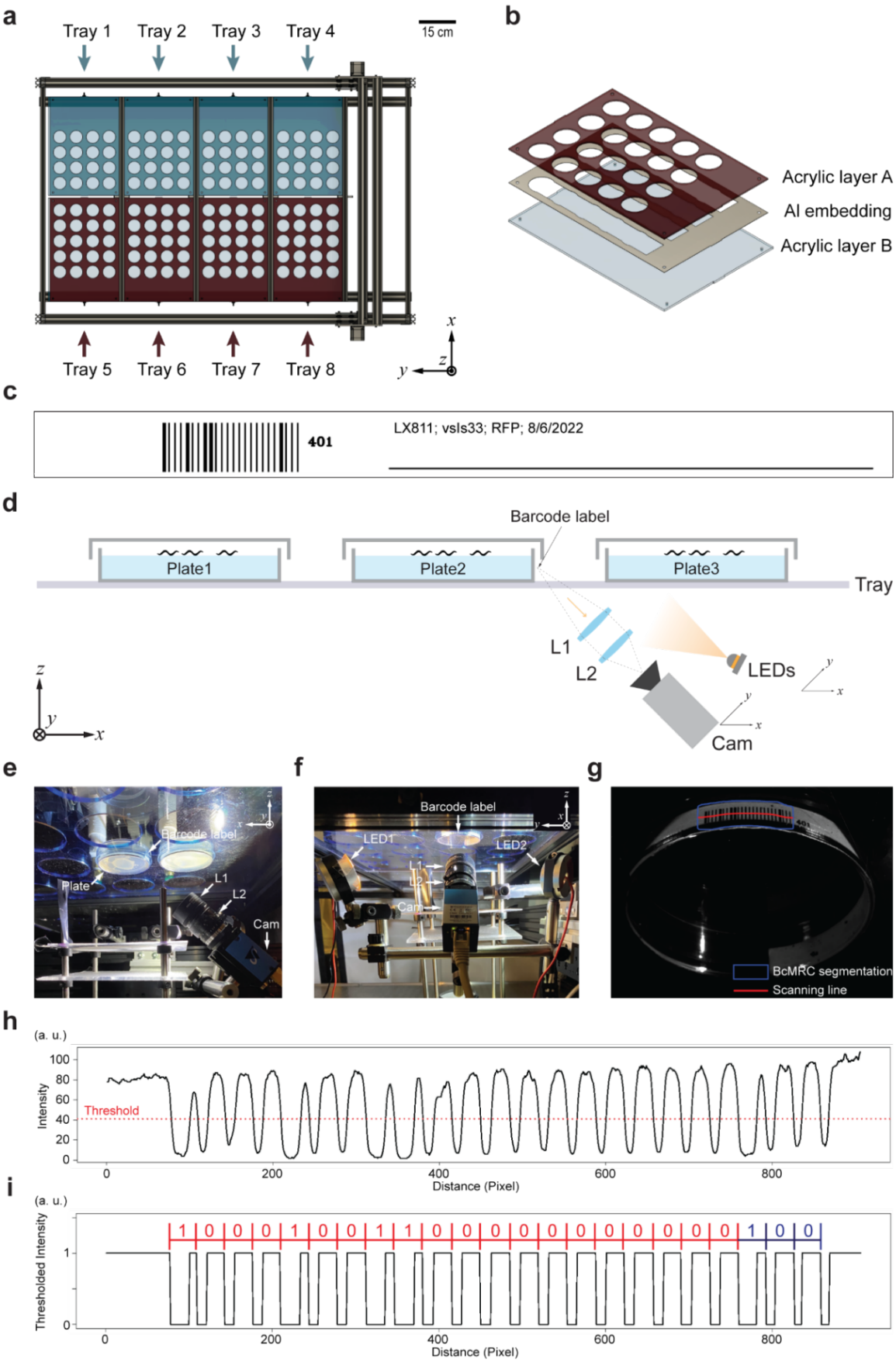

Supplementary Fig. 2 | Plate tray platform. a. Top view of WormPicker plate tray platform. The platform is composed of eight easy slide-in plate trays, with arrows indicating the slide-in directions. **b**. Each slide-in plate tray consists of two transparent laser-cut acrylics sandwiching an aluminum embedding layer. **c**. Image of barcode label. **d**. Schematic of machine vision system for barcode label reading. **e**-**f**, Front and side view photographs of the machine vision apparatus for reading the barcode label. **g**. Camera-captured image of the label with the highlighted BcMRC-segmented barcode region and the barcode scanning line. **h**. Profile of the pixel intensity along the barcode scanning line depicted in **g**. Red dash-line: threshold for binarizing the intensity profile. **i**. The intensity profile after being binarized by the threshold depicted in **h**. The decoded 20-bit number (red) and the 3-bit checksum (blue) are marked above.

Supplementary Fig. 3 Imaging and manipulation assemblies

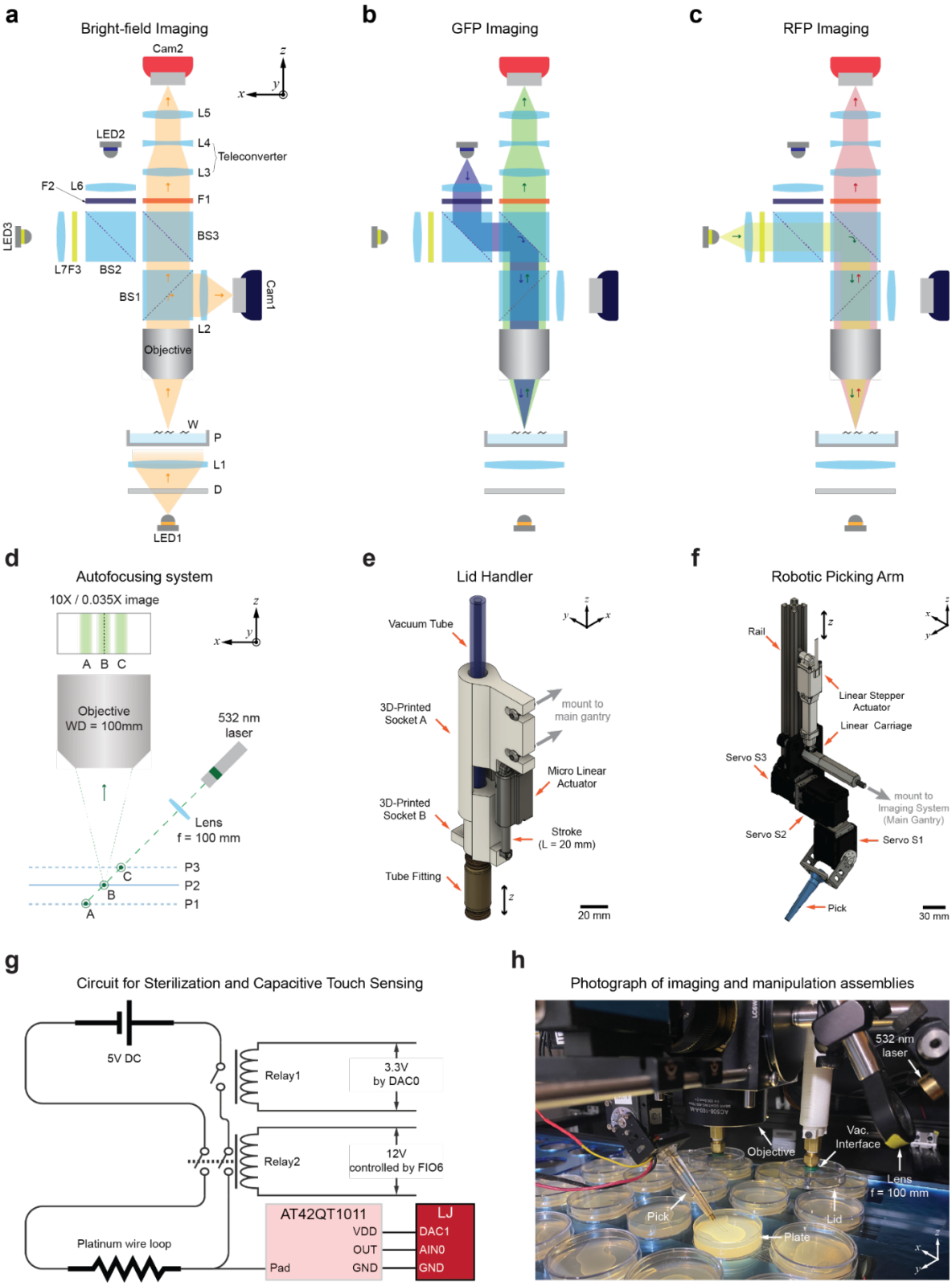

Supplementary Fig. 3 | Imaging and manipulation assemblies. a-c. Schematic of the bright-field (**a**), GFP (**b**), and RFP (**c**) imaging. BS1: beamsplitter (transmission : reflection = 90% : 10%) BS2-3:

dichroic beamsplitters. Cam1: machine vision camera. Cam2: CMOS camera. D: Optical diffuser. F1-3: spectrum filters. L1: Fresnel lens. L2: machine vision camera lens. L3-5: achromatic doublet lenses. L6-7: condenser lenses. LED1: white LED. LED2: 470 nm LED. LED3: 565 nm LED. Objective: achromatic doublet lens (f = 100 mm). P: agar plate. W: worms. **d**. Schematic of the autofocusing system. P1-3: different positions of the agar surface; A-C: positions of the laser projected to the agar surface at different planes, i.e., P1-3. Dashed line: the optimal x position. **e**. Schematic of the lid handler. **f**. Schematic of the robotic picking arm. **g**. Electric circuit for the pick sterilization and the capacitive touch sensing. AT42QT1011: capacitive touch sensor; LJ: LabJack **h**. Photograph of the imaging and manipulation assemblies.

Supplementary Fig. 4 Pick focus control

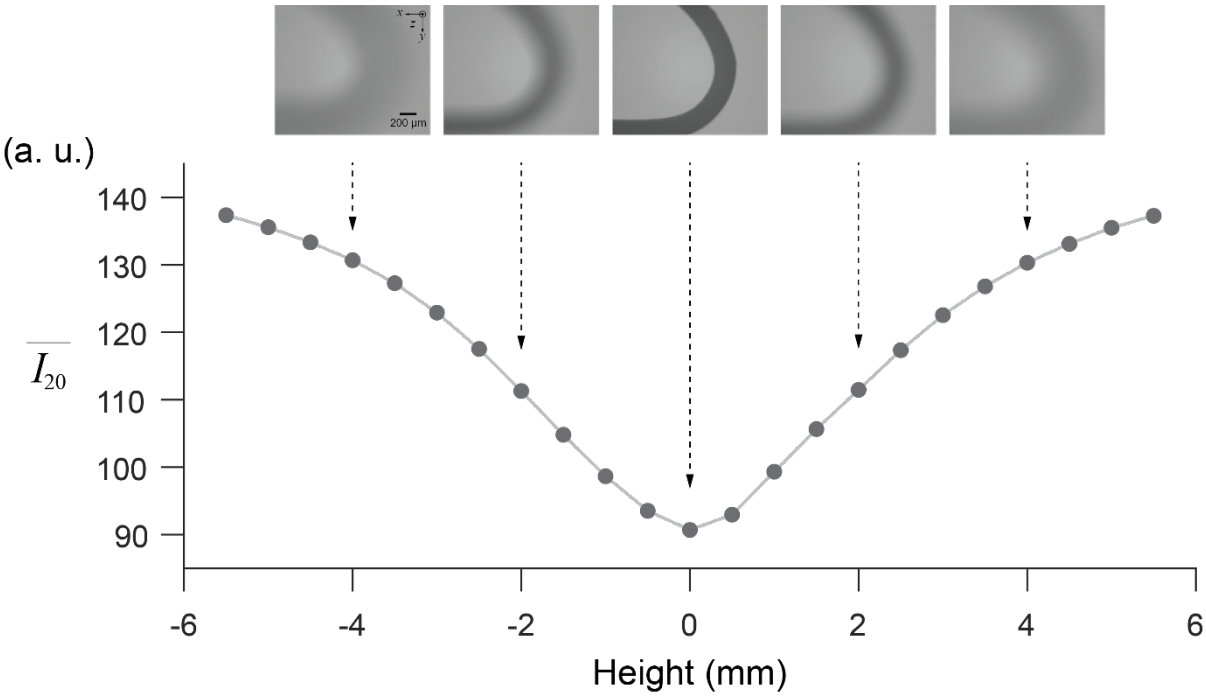

Supplementary Fig. 4 | Pick focus control. The wellness of the wire pick focus is quantified by the mean intensity of top 20% darkest pixels of the high-magnification images $\overline{I_{20}}$. The figure depicts how $\overline{I_{20}}$ changes along with the height of the wire pick. The x axis is the height of the pick, where the height at which the pick is well focused is set to zero, and the y axis the $\overline{I_{20}}$. The pictures shown

above the plot are pick images captured at different heights, with dashed line arrows pointing to the corresponding points in the graph.

Supplementary Fig. 5 Machine vision analysis

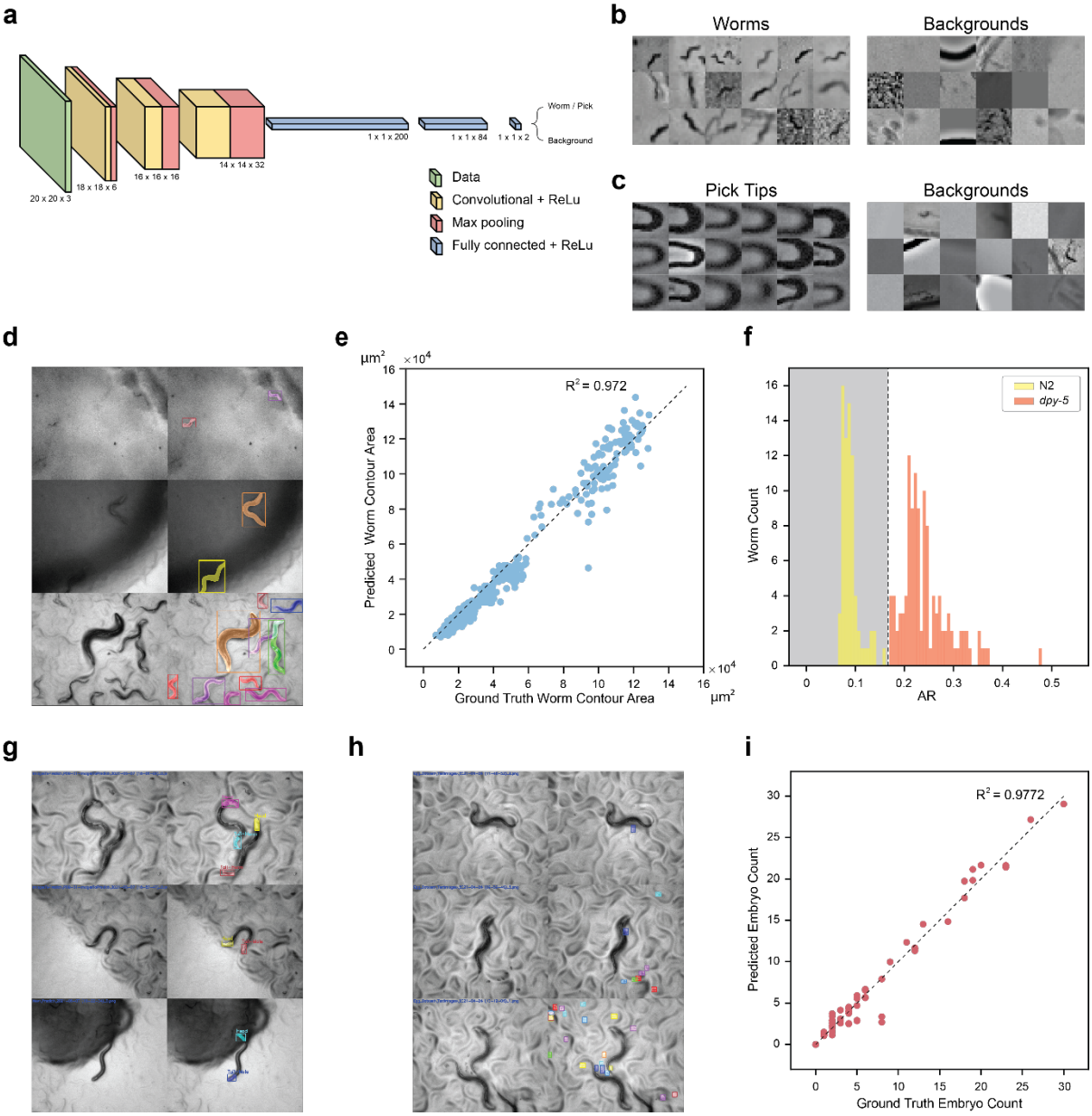

Supplementary Fig. 5 | Machine vision analysis. a. Structure of WormCNN and PickCNN. **b**. Representative images of worms (left) and backgrounds (right) for WormCNN training. **c**. Representative images of pick tips (left) and backgrounds (right) for PickCNN training. **d**. Worm segmentations by WorMRC (left: raw images; right: segmentations). FOV: 1.88 x 1.57 mm. Individual

worms are labeled with different colors. **e**. Areas of individual worm contours (of mixed stages, L1-Adult) segmented by the WorMRC shows high consistency with the ground truth ($R^2 = 0.972$, N = 690). The black dashed line: $y = x$. **f**. Morphological analysis. The histogram shows the aspect ratios (AR) for wild-type (N2) and Dpy (*dpy-5*) animals (N = 190). Decision boundary (black dash-line) is shown for classifying wild-type (gray region) and dumpy morphology (white region). **g**. Sex determination by SexMRC (left: raw images; right: segmentations). Individual heads and tails are labeled with different colors. Recognized tail types are indicated by the texts. **h**. Embryo detection by EmbMRC (left: raw images; right: segmentations). Individual embryos or clusters of embryos are labeled with different colors. **i**. Number of embryos detected by the EmbMRC shows high consistency with the ground truth ($R^2 = 0.9772$, N = 124). The black dashed line: $y = x$.

Supplementary Fig. 6 Manual and automated picking throughputs

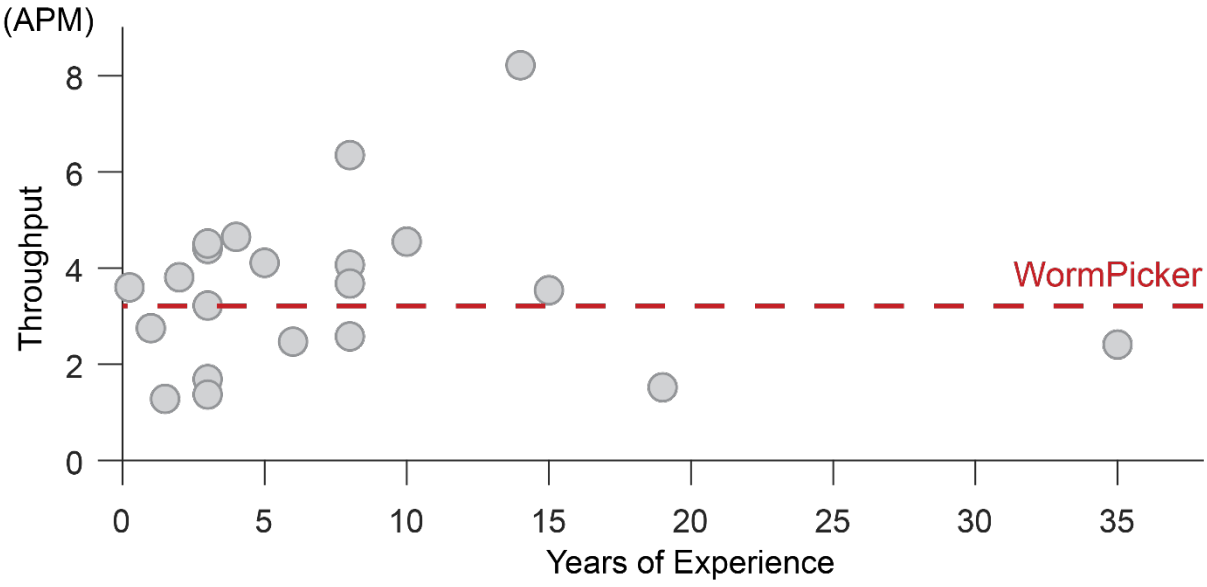

Supplementary Fig. 6 | Manual and automated picking throughputs. We recruited a group of *C. elegans* researchers (N = 21) with different levels of experience to perform a fluorescent animal sorting task. The measured picking throughput (unit: Animal per Minute, APM) are plot against the years of experience for each participant (gray points). The mean and median of the years of

experience are 7.61 and 5 years. The mean, median, and standard deviation (SD) of the measured manual throughput are 3.56, 3.60, and 1.67 APM. The red dash-line indicates the measured automated throughput, 3.21 APM (SD = 0.66 APM, N = 38).

Supplementary Fig. 7 Schematic of WormPickerControl and WormPickerLib

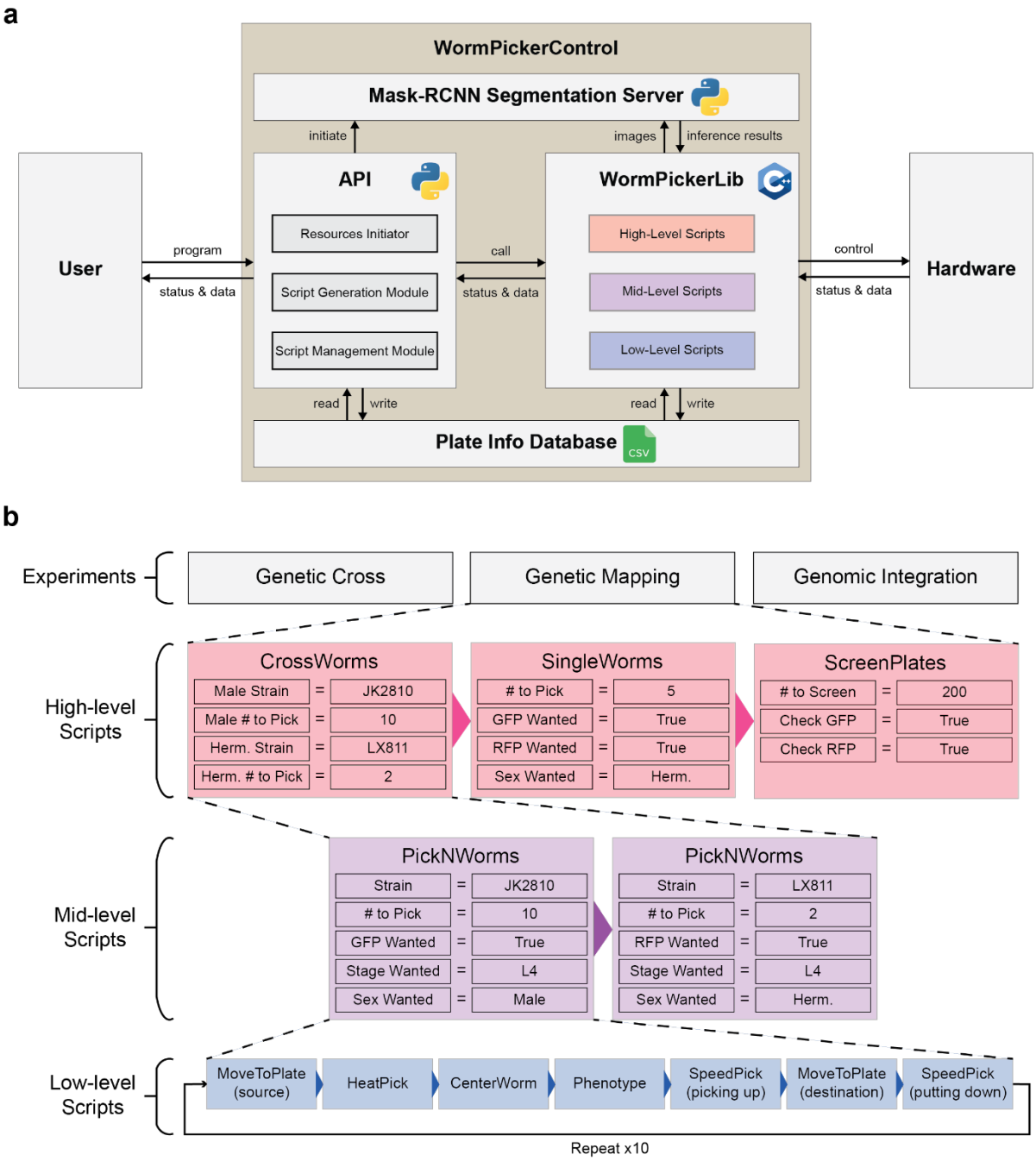

Supplementary Fig. 7 | Schematic of WormPickerControl and WormPickerLib. a. Schematic of

WormPicker system control software WormPickerControl. WormPickerControl is composed of four modules, including an Application Programming Interface (API), WormPickerLib (a library of source scripts), a Mask-RCNN segmentation server, and a database cataloging plate information. **b**. An example of WormPickerLib call stack for performing a specific genetic experiment in this study: determine linkage to chromosomes I and III for an RFP transgene *vsIs33* (Fig. 4c), demonstrating the hierarchical architecture of WormPickerLib.

Supplementary Fig. 8 Theory of I/III-linkage test

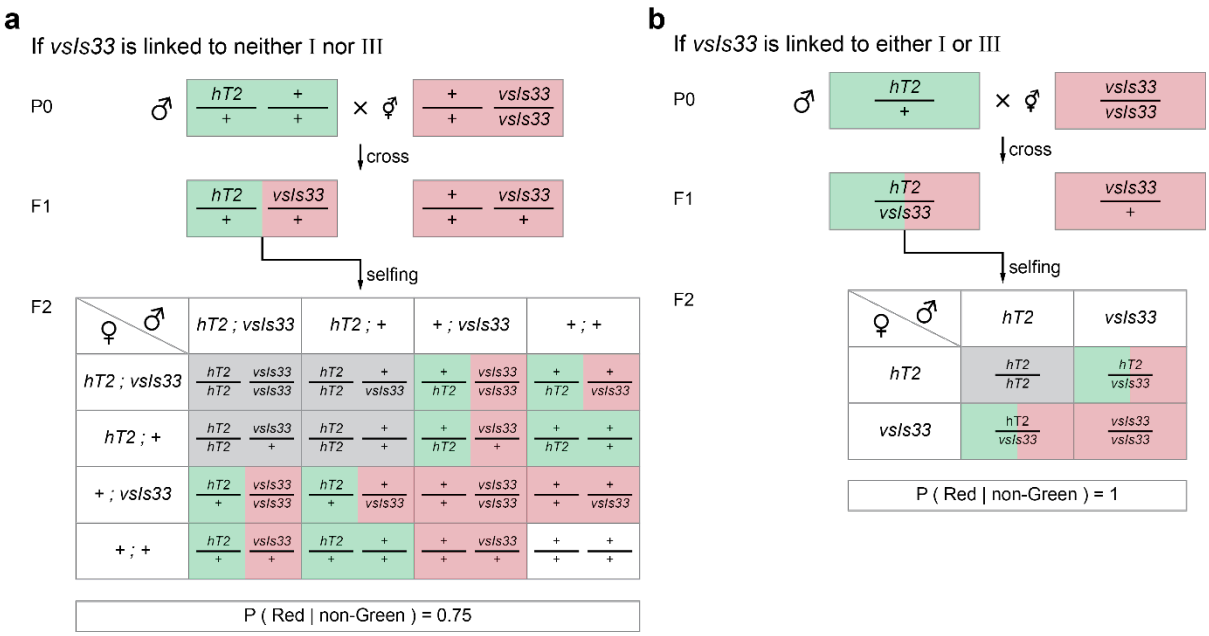

Supplementary Fig. 8 | Theory of I/III-linkage test. a. Punnett square depicting the predicted F2s to be observed supposing *vsIs33* linked to neither I nor III. Colors indicate types of fluorescent reporters can be observed for each genotype: Green for GFP and Red for RFP. Gray indicates the lethality due to homozygous *hT2*. It is anticipated to observe 75% of the non-Green F2s would be Red. **b**. Punnett square depicting the predicted F2s to be observed supposing *vsIs33* linked to either I or III. Color code same as **a**. It is anticipated to observe 100% of the non-Green F2s would be Red.

Supplementary Fig. 9 Theory of II-linkage test

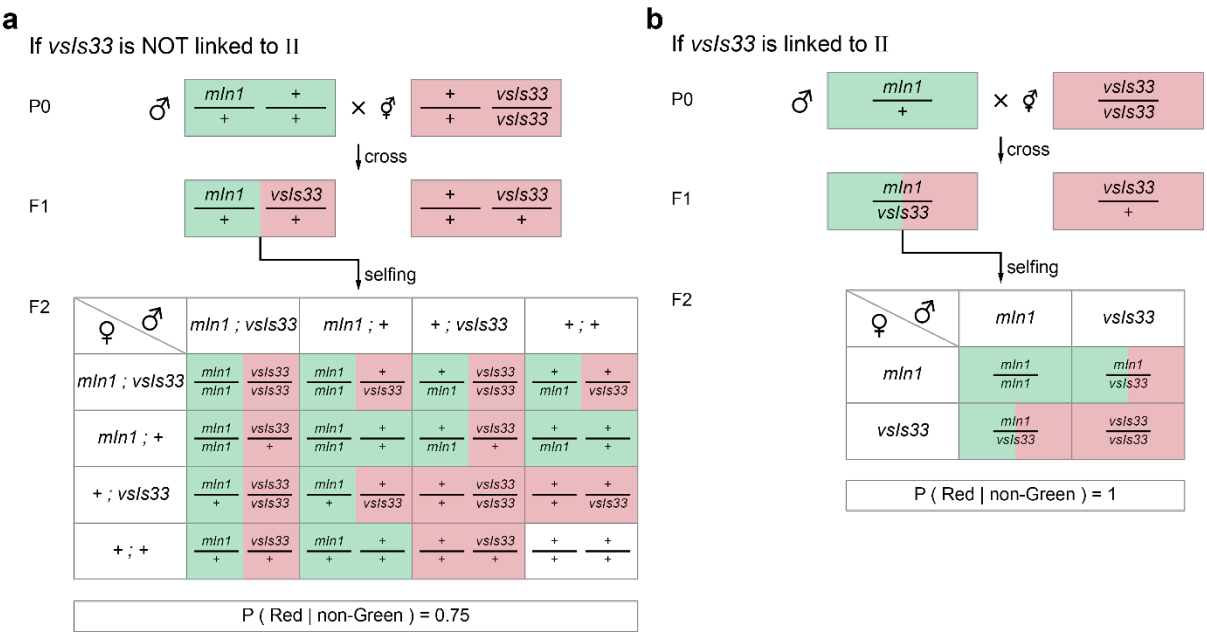

Supplementary Fig. 9 | Theory of II-linkage test. a. Punnett square depicting the predicted F2s to be observed supposing *vsIs33* not linked to II. It is anticipated to observe 75% of the non-Green F2s would be Red. **b**. Punnett square depicting the predicted F2s to be observed supposing *vsIs33* linked to II. It is anticipated to observe 100% of the non-Green F2s would be Red. For **a** and **b**, color code same as Supplementary Fig. 8a.

Supplementary Fig. 10 Theory of III/V-linkage test

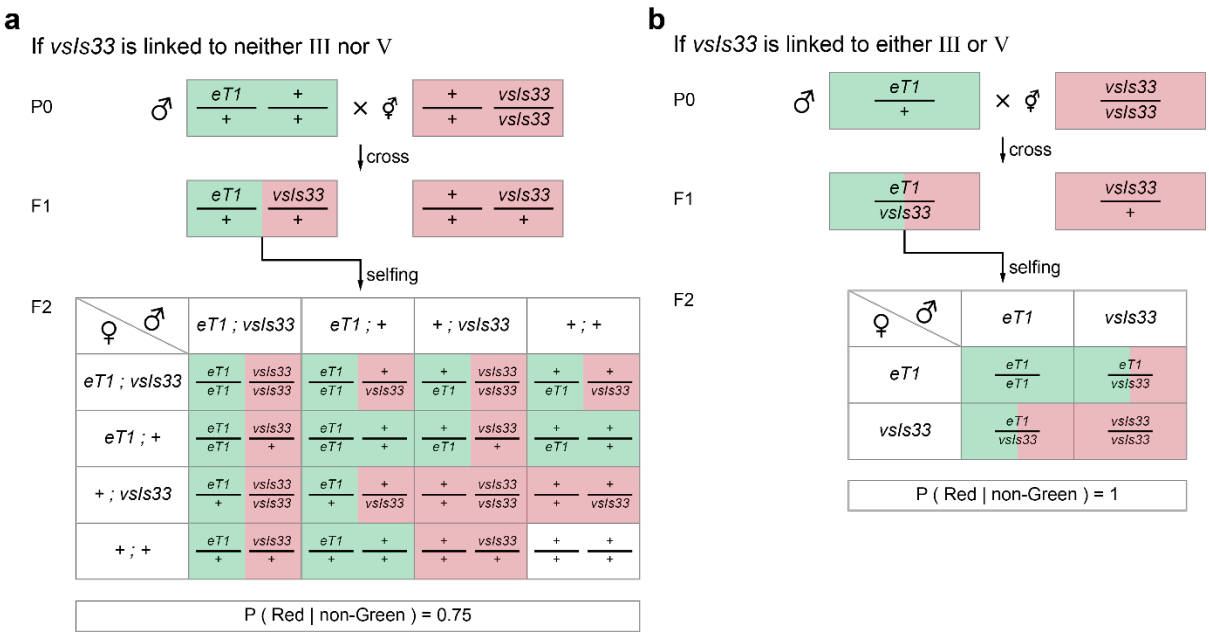

Supplementary Fig. 10 | Theory of III/V-linkage test. a. Punnett square depicting the predicted F2s to be observed supposing *vsIs33* linked to neither III nor V. It is anticipated to observe 75% of the non-Green F2s would be Red. **b**. Punnett square depicting the predicted F2s to be observed supposing *vsIs33* linked to either III or V. It is anticipated to observe 100% of the non-Green F2s would be Red. For **a** and **b**, color code same as Supplementary Fig. 8a.

Supplementary Fig. 11 Theory of IV/V-linkage test

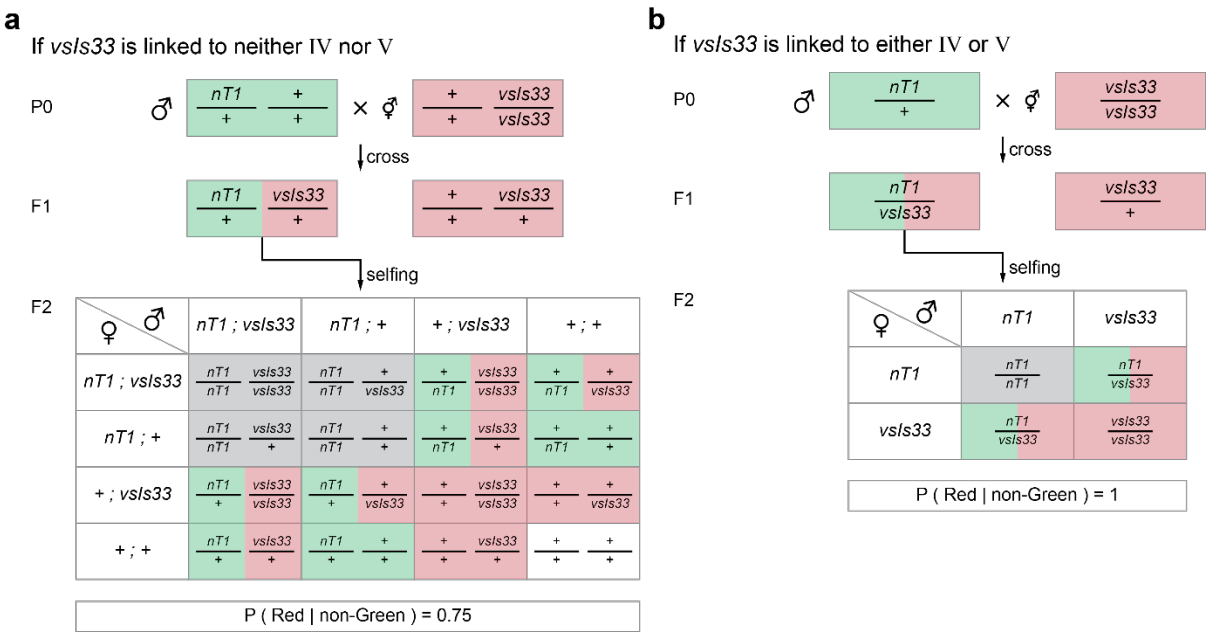

Supplementary Fig. 11 | Theory of IV/V-linkage test. a. Punnett square depicting the predicted F2s to be observed supposing *vsIs33* linked to neither IV nor V. It is anticipated to observe 75% of the non-Green F2s would be Red. **b**. Punnett square depicting the predicted F2s to be observed supposing *vsIs33* linked to either III or V. It is anticipated to observe 100% of the non-Green F2s would be Red. For **a** and **b**, color code same as Supplementary Fig. 8a.

Supplementary Fig. 12 Theory of X-linkage test

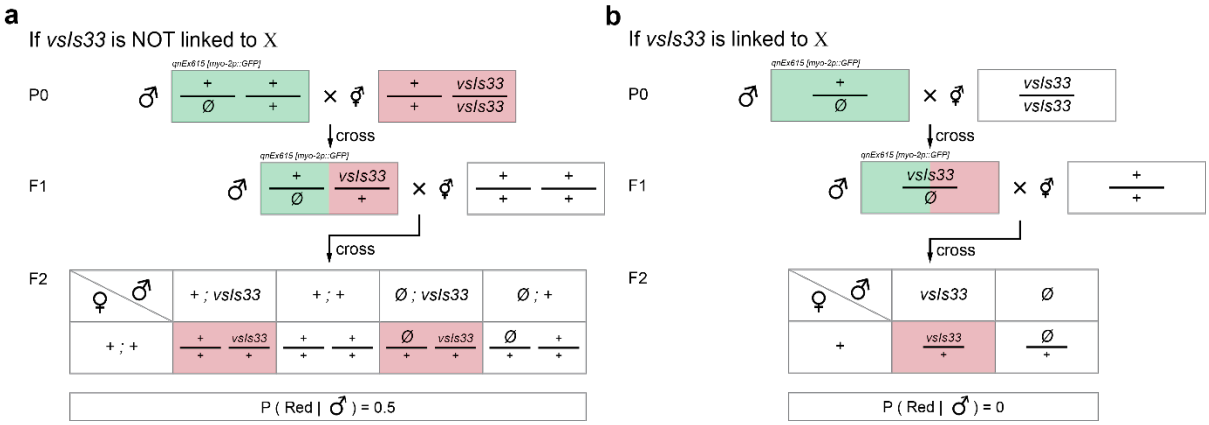

Supplementary Fig. 12 | Theory of X-linkage test. a. Punnett square depicting the predicted F2s to be observed supposing *vsIs33* not linked to X. It is anticipated to observe 50% of the F2 males would

be Red. **b**. Punnett square depicting the predicted F2s to be observed supposing *vsIs33* linked to X. It is anticipated to observe none of the F2 males would be Red. For **a** and **b**, color code same as Supplementary Fig. 8a.

Supplementary Fig. 13 Linkage of vsIs33 over chromosomes

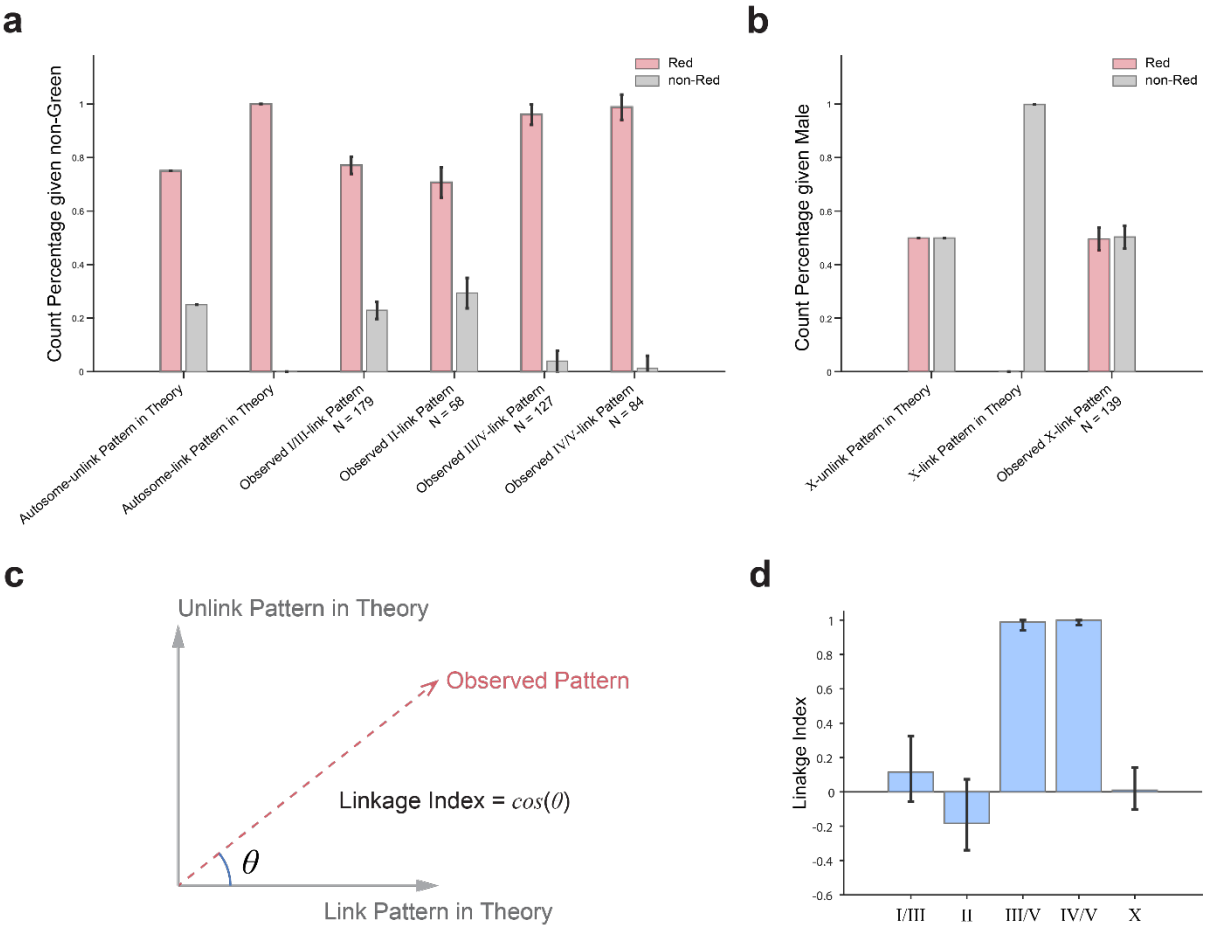

Supplementary Fig. 13 | Linkage of *vsIs33* over chromosomes. a. Theory predicted and the observed count percentages of Red and non-Red among the non-Green F2s for determining linkage of *vsIs33* to autosomes. Error bar indicates one standard deviation higher and lower than the observed percentage under the autosomal unlink assumption. **b**. Theory predicted and the observed count percentages of Red and non-Red among the F2 males for determining linkage of *vsIs33* to the X chromosome. Error bar indicates one standard deviation higher and lower than the observed percentage under the X-unlink assumption. **c**. Graphical representation of the Linkage Index. **d**.

Observed Linkage Indices for *vsIs33* over different chromosomes. The upper and lower bounds of the error bars correspond to the Linkage Indices calculated when one standard deviation higher and lower than the observed percentages, matching the error bars in **a** and **b**.

Supplementary Table 1 WormPicker key components list

Figure ID		**Part**	**Description**	**Part Number (Vendor)**
Fig. 1	**c**	Contact pin	Contact Pin 14-18AWG Crimp	N.A.
		Platinum wire loop	90% Platinum, 10% Iridium Wire	PT-9010 (Tritech Research)
Supplementary Fig. 1	**Externals**	PC	PC, Intel(R) Core i9-10900K CPU@3.7 GHz, 64 GB RAM, GPU NVIDIA QuADro P1000	(Origin)
	Motion System	Timing Belt	3GT (GT2-3M) Timing Belt	(OpenBuilds)
		Lead Screw	8mm Metric Acme Lead Screw	(OpenBuilds)
		X/Y/Z Limit Switch	Xtension Limit Switch Kit	(OpenBuilds)
		X/Y/Z Stepper Motor	NEMA 23 Stepper Motor	(OpenBuilds)
	Plate Tray	Agar Plate	60mm vented, sharp edge Petri Dishes	T3315 (Tritech Research)

Supplementary Fig. 2	**b**	Al embedding	Aluminum foil (16.26 μm thick)	Reynolds Wrap (Amazon)
	d	Cam	Machine vision camera	DMK33GP031 (Imaging Source)
		L1	Achromatic Doublet (f = 75 mm, Ø1")	AC254-075-A-ML (Thorlabs)
		L2	Machine vision lens (f = 8 mm)	N.A.
		LEDs	High Intensity LED Flood (Warm White 3000-3200K, 120 lm)	(Oznium)
Supplementary Fig. 3	**a**	BS1	UVFS Plate Beamsplitter (Ø2" 10:90 (R:T), Coating: 400-700 nm, t = 8 mm)	BSN16 (Thorlabs)
		BS2	Long-pass Dichroic beamsplitter	XF2010 (Omega Optical)
		BS3	Dual-band Dichroic beamsplitter	59022bs (Chroma)
		Cam1	Machine vision camera	DMK33GP031 (Imaging Source)
		Cam2	Monochrome CMOS Camera (Kiralux 5.0 MP, 53.2 fps Max)	CS505MU (Thorlabs)
		D	Optical diffuser (Acrylic Sheet Lucite Plexiglass, Clear P95 Frost Light Transmission 90%)	(Rock Hard Plastics)

		F1	Dual-band emission filter	59022m (Chroma)
		F2	Excitation filter	XF2015 (Omega Optical)
		F3	Excitation filter	65-705 (Edmund Optics)
		L1	Fresnel lens (5" x 5", 4" Focal Length)	(Edmund optics)
		L2	Machine vision lens (f = 3.5 mm)	T3Z3510CS (Computar)
		L3	Achromatic Doublet Lens (f = 300 mm, Ø1", ARC: 400-700 nm)	AC254-300-A-ML (Thorlabs)
		L4	Achromatic Doublet Lens (f = -100 mm, Ø1", ARC: 400-700 nm)	ACN254-100-A (Thorlabs)
		L5	Achromatic Doublet Lens (f = 150 mm, Ø1", ARC: 400-700 nm)	AC254-150-A-ML (Thorlabs)
		L6	Collimation Module for LEDs with 80° to 120° Divergence Angle	SFM80 (Thorlabs)
		L7	Aspheric Condenser Lens (f=20.1 mm, Ø25 mm, NA = 0.60, ARC: 350-700 nm)	ACL2520U-A (Thorlabs)
		LED1	High Intensity LED Flood (Warm White 3000-3200K, 120 lm)	(Oznium)

		LED2	LED (470 nm)	M470L5 (Thorlabs)
		LED3	LED (565 nm)	M565L3 (Thorlabs)
		Objective	Achromatic doublet lens (f = 100 mm, Ø2", ARC: 400-700 nm)	AC508-100-A-ML (Thorlabs)
	d	Laser	Green Cross Laser LINE Generator	Quarton Laser Module VLM-532-47 LPT (Amazon)
		Lens	N-BK7 Plano-Convex Lens (Ø1", f = 100 mm)	LA1509-A (Thorlabs)
	e	Micro Linear Actuator	PQ12-S Linear Actuator with Limit Switches 30:1 12 volts	PQ12-30-12-S (Actuonix)
		Vacuum Interface	Push-to-Connect Tube Fittings	51025K196 (McMaster-Carr)
		Vacuum Tube	High-Pressure Soft Plastic Tubing for Air and Water	52375K11 (McMaster-Carr)
	f	Linear Carriage	Mini V Gantry Kit	(OpenBuilds)
		Linear Stepper Actuator	50mm S20 Stepper Actuator	S20-30-38-B (Actuonix)
		Rail	V-Slot® 20x20 Linear Rail, Length = 250 mm	(OpenBuilds)

		Servo S1-3	MX-28T Robot Actuator	RO-902-0067-000 (Trossen Robotics)
	g	AT42QT1011	Capacitive Touch Breakout	AT42QT1011 (SparkFun)
		Relay 1	SE Relays, solid state, SPST NO, 25A, Output 3-200 VDC, Input 3-32 VDC	6325AXXMDS-DC3 (Schneider)
		Relay 2	General Purpose Relay DPDT 10A 12VDC	1885-1706-ND (Digi-Key)

1237 **Supplementary Table 2 Pick motion trajectory parameters**

Picking up										
Phase	**Lin. Step. Act.**		**Servo S1**		**Servo S2**		**Servo S3**		**Main Gantry**	
	Velocity in z (mm/s)	Displacement in z (mm)	Angular Velocity (deg/s)	Angular Displacement (deg)	Angular Velocity (deg/s)	Angular Displacement (deg)	Angular Velocity (deg/s)	Angular Displacement (deg)	Velocity in z (mm/s)	Displacement in z (mm)
A	-20	-2.5	0	0	0	0	0	0	0	0
B	0	0	0	0	274.8	1.23	0	0	0	0
C	0	0	274.8	0.44	0	0	274.8	0.44	0	0
Putting down										
Phase	**Lin. Step. Act.**		**Servo S1**		**Servo S2**		**Servo S3**		**Main Gantry**	
	Velocity in z	Displacement in z	Angular Velocity	Angular Displacement	Angular Velocity	Angular Displacement	Angular Velocity	Angular Displacement	Velocity in z	Displacement in z

	(mm/s)	(mm)	(deg/s)	nt (deg)	(deg/s)	nt (deg)	(deg/s)	nt (deg)	(mm/s)	(mm)
A	-20	-2.5	0	0	0	0	0	0	0	0
A-B waiting (s)	1									
B	0	0	0	0	-274.8	-1.58	0	0	0	0
B-C waiting (s)	2									
C	0	0	0	0	0	0	0	0	-125	-0.4
D	0	0	274.8	39.11	0	0	0	0	0	0

Supplementary Table 3 Fluorescence imaging and processing parameters

Experiment	Purpose	Fluorescent transgene of interest	GFP imaging parameters				RFP imaging parameters			
			Exposure (ms)	Intensity threshold (a. u.)	Area threshold (pixel^2)	Iteration	Exposure time (ms)	Intensity threshold (a. u.)	Area threshold (pixel^2)	Iteration
Genetic Cross (Fig. 3)	Assay transgene expression	*vsIs28 [dop-1p::GFP]*	200	70	20	N.A.				
Genetic Mapping (Fig. 4)	Test I/III-linkage	*vsIs33 [dop-3p::RFP]*					100	80	20	N.A.

		hT2 {qIs48 [myo-2::GFP]}	200	80	20	N.A.				
	Test II-linkage	*vsIs33 [dop-3p::RFP]*					100	80	50	50
		mIn1 {mIs14 [myo-2::GFP]}	200	60	50	50				
	Test III/V-linkage	*vsIs33 [dop-3p::RFP]*					100	60	20	100
		eT1 {umnIs12 [myo-2::GFP]}	200	130	20	100				
	Test IV/V-linkage	*vsIs33 [dop-3p::RFP]*					100	80	20	50
		nT1 {qIs51 [myo-2::GFP]}	200	80	20	50				
	Test X-linkage	*vsIs33 [dop-3p::RFP]*					100	80	20	N.A.
		qnEx615 [myo-2p::GFP]	200	80	20	N.A.				
Genomic integration of transgene (Fig. 5)	Assay transgene expression	*qhEx265 [unc-47p::GFP]*	200	70	1	50				

1240 **Supplementary Table 4 WormPickerLib: Script library of common**

1241 ***C. elegans* procedures**

Category	Name	Description
High-level	CrossWorms	Pick hermaphrodites and males matching specified phenotypes from two source plates into one destination plate
	ScreenPlates	Screen multiple plates for assaying population phenotypes
	SingleWorms	Pick worms matching specified phenotypes to individual plates. A single worm per plate.
Mid-level	PickNWorms	Pick multiple worms matching specific phenotypes from one plate to another
	ScreenOnePlate	Screen a single plate for assaying population phenotypes
Low-level	AutoFocus	Focus the images
	CalibOx	Calibrate how many pixel-translations in the image corresponding to one unit movement in the gantry
	CalibPick	Calibrate the pick position in the low-magnification FOV. Mapping the pick tip positions with servo coordinates
	CalibTray	Calibrate the well positions over the plate tray platform
	CenterWorm	Track worms and move individual animals to the high-magnifcation FOV
	HeatPick	Sterilize the pick
	MoveToPlate	Move the gantry above a plate
	Phenotype	Phenotype any worms found in the high-magnification images
	ReadBarCode	Read the barcode identifier on the plate, write/read the plate information to/from the database
	SpeedPick	Perform a single picking up/putting down action on the agar surface

1242 **Supplementary Table 5 Strains used in this study**

Designation	Source or reference	Identifiers	Additional information
OP50	CGC	Fang-Yen Lab Strain Collection: OP50 RRID:WB-STRAIN:WBStrain00041971	OP50
CB61	CGC	Fang-Yen Lab Strain Collection: CB61	dpy-5(e61) I.
CGC34	Gift of D. Raizen	Fang-Yen Lab Strain Collection: CGC34	eT1 [umnIs12] III; eT1 V.
JK2810	Gift of D. Raizen	Fang-Yen Lab Strain Collection: JK2810	mcm-4(e1466) dpy-5(e61)/hT2 I; dpy-18(e364) III/hT2 [bli-4(e937) let-?(q782) qIs48] (I;III).
JK2958	Gift of D. Raizen	Fang-Yen Lab Strain Collection: JK2958	nT1 [qIs51] (IV;V)/dpy-11(e224) unc-42(e270) V.
LX811	CGC	Fang-Yen Lab Strain Collection: LX811	vsIs33 V; lin-15B&lin-15A(n765) X.
LX831	CGC	Fang-Yen Lab Strain Collection: LX831	vsIs33 V; lin-15B&lin-15A(n765) X; vsIs28.
N2	CGC	Fang-Yen Lab Strain Collection: N2	wild-type
NQ1155	Gift of D. Raizen	Fang-Yen Lab Strain Collection: NQ1155	qnEx615 [myo-2p::GFP]
VC170	Gift of D. Raizen	Fang-Yen Lab Strain Collection: VC170	cki-1(gk132)/mIn1 [dpy-10(e128) mIs14] II.
YX256	Gift of P. McClanahan	Fang-Yen Lab Strain Collection: YX256	syEx723 [hs::LIN-3C; myo-2::GFP; pha-1(+)]
YX293	Gift of H. Ji	Fang-Yen Lab Strain Collection: YX293	dop-3(vs106); qhEx265 [acr-2p::DOP-3(+) + unc-

			47p::GFP]
YX300	Crossed LX831 with CB61	Fang-Yen Lab Strain Collection: YX300	vsIs28 [dop-1p::GFP]; dpy-5 (e61) I.
YX301	UV integration of YX293	Fang-Yen Lab Strain Collection: YX301	dop-3(vs106); qhIs12 [acr-2p::DOP-3 + unc-47p::GFP]
YX302	UV integration of YX293	Fang-Yen Lab Strain Collection: YX302	dop-3(vs106); qhIs13 [acr-2p::DOP-3 + unc-47p::GFP]

Supplementary Video 1 Automated multimodal fluorescence imaging in *C. elegans*

Supplementary Video 1 | Automated multimodal fluorescence imaging in *C. elegans.*

Transgenic (JK2958) *C. elegans* in bright-field images followed by an image from the GFP channel. Transgenic (LX811) *C. elegans* in bright-field images followed by an image from the RFP channel. FOV: 1.88 mm x 1.57 mm.

Supplementary Video 2 Lid manipulation

Supplementary Video 2 | Lid manipulation. Lids of agar plates on the platform are removed and replaced using two motorized vacuum actuators.

Supplementary Video 3 Pick sterilization

Supplementary Video 3 | Pick sterilization. The platinum wire loop pick is sterilized by resistive heating.

Supplementary Video 4 Automated *C. elegans* picking from the camera view

Supplementary Video 4 | Automated *C. elegans* picking from the camera view. Overlay of the high-magnification and low-magnification video streams. A worm is automatically picked up by the wire loop pick and transferred to a different plate.

Supplementary Video 5 Automated *C. elegans* transfer between agar substrates, external view

Supplementary Video 5 | Automated *C. elegans* transfer between agar substrates. An electric current sterilizes the pick; worms are tracked and phenotyped; the robotic arm picks up a worm from a plate and transfers it to a second plate.